ANALYSIS AND CORRECTION OF THREE-DIMENSIONAL PROXIMITY EFFECT IN BINARY E-BEAM NANO-LITHOGRAPHY

Except where reference is made to the work of others, the work described in this thesis is my own or was done in collaboration with my advisory committee. This thesis does not include proprietary or classified information.

Kasi Lakshman Karthi, Anbumony

Certificate of Approval:

Stanley J. Reeves
Professor
Electrical and Computer Engineering

Soo-Young Lee, Chair
Professor
Electrical and Computer Engineering

Ramesh Ramadoss
Assistant Professor
Electrical and Computer Engineering

Joe F. Pittman
Interim Dean
Graduate School

ANALYSIS AND CORRECTION OF THREE-DIMENSIONAL PROXIMITY EFFECT IN BINARY E-BEAM NANO-LITHOGRAPHY

Kasi Lakshman Karthi, Anbumony

A Thesis

Submitted to

the Graduate Faculty of

Auburn University

in Partial Fulfillment of the

Requirements for the

Degree of

Master of Science

Auburn, Alabama
May 10, 2007

Analysis and Correction of Three-Dimensional Proximity Effect in Binary E-beam Nano-Lithography

Kasi Lakshman Karthi, Anbumony

Signature of Author

Date of Graduation

VITA

Kasi Lakshman Karthi, Anbumony was born in Nagercoil, Kanyakumari District, Tamil Nadu, India on November 26, 1982. He entered the Hindustan College of Engineering, University of Madras in 2000 and received a B.E. with honors in Electronics and Communication Engineering in 2004. In August 2004, he started his graduate career in Auburn University, completing his M.S. in Electrical and Computer Engineering in December 2006.

Thesis Abstract

Analysis and Correction of Three-Dimensional Proximity Effect in Binary E-beam Nano-Lithography

Kasi Lakshman Karthi, Anbumony

Master of Science, May 10, 2007
(B.E., University of Madras in India, 2004)

101 Typed Pages

Directed by Soo-Young Lee

One of the fundamental problems in transferring a circuit pattern onto a substrate using electron beam lithography is the *proximity effect*, which is due to electron scattering in the resist and results in the "non-ideal" distribution of exposure (*energy deposited* in the resist) leading to the blurring of the written circuit pattern. For high-density circuit patterns with fine features of nanometer scale, the proximity effect can become so severe that features may merge if not corrected for the effect. All of the previous proximity effect correction schemes used a two-dimensional (2-D) exposure model for proximity effect correction by ignoring or averaging the variation of exposure along the depth dimension in the resist. In this thesis, the three-dimensional (3-D) proximity effect correction for *binary lithography* is addressed with emphasis on sidewall shape. The objective of 3-D correction is to control electron beam dose distribution within each circuit feature using a 3-D *point spread function* (PSF) in order to achieve a certain desired remaining resist profile after development.

As the first step towards developing 3-D proximity effect correction schemes, two prototype versions, 3-D *iso-exposure contour correction* and 3-D *resist profile correction*, have been implemented in this thesis. The main purpose of these prototype implementation is to demonstrate the efficiency of real 3-D correction and, therefore, the iso-exposure contours and resist profiles of certain cross-sections in one direction only are considered in these versions. The 3-D resist profile correction leads to more realistic results in general since it takes the resist development process into account.

Through computer simulations, the 3-D proximity effect and performance of the 3-D correction methods have been analyzed for simple patterns such as a single and three-line patterns.

ACKNOWLEDGMENTS

I would like to thank my advisor Dr. Soo-Young Lee for all his support, detailed guidance and many helpful suggestions throughout the entire development of PYRAMID for three-dimensional lithography without which this thesis would not have been possible. I would also like to thank the other members of my committee, Dr. Stanley J. Reeves and Dr. Ramesh Ramadoss for their help and support. Thanks are also due to the National Science Foundation followed by Seagate Technology for funding this research and to Auburn University and Department of ECE for their financial support. I would also like to thank Dr. Fei Hu for helping me get familiar with the previous PYRAMID programs. Last but not least, I would like to thank my family, my friends and all other people who have given me help during my M.S. study.

To my loved family members and heavenly abodes, without whose support I would not be able to be where I am now.

Style manual or journal used Bibliography conforms to those of the transactions of the Institute of Electrical and Electronics Engineers

Computer software used LaTeX typesetting language with aums style file developed by the Auburn University Department of Mathematics

TABLE OF CONTENTS

List of Figures

LIST OF TABLES

Chapter 1

Introduction

Electron beam (e-beam) lithography is one of the key techniques to transfer circuit patterns onto silicon or other substrates. It uses a focused electron beam to expose a pattern on a sensitive material (the *resist*) applied to the surface of the substrate. *Proximity effect* is caused by forward and backward scattering of electrons after they enter the resist and subsequent reflection from the substrate, which results in undesirable blurring and degradation in the written circuit pattern. The degree of scattering depends on the energy of electrons, the effective atomic number of the substrate materials, and the thickness of the resist, etc. [28–30]. For circuit patterns with very fine features, proximity effect can cause blurring of features or the neighboring features even to merge. The main problem due to proximity effect in fabrication of a grayscale structure is the non-uniform *exposure* (energy deposited per unit area) distribution within each feature, which would lead to an uneven surface of the corresponding region after the fabrication process and of a binary structure (circuit pattern) is that features may blur out or shrink into their ideal boundaries.

As the circuit size and density continue to increase and the *minimum feature size* (MFS) steadily shrinks, proximity effect is expected to impose an increasingly serious limitation on fabrication of binary structures. Therefore, an effective method to control *dose* (energy given per unit area) in the lithographic process for fabricating structures is to be developed.

1.1 Previous Work

The issues of proximity effect correction has been steadily investigated by many researchers since the 1970's [29–39]. In general, they use *dose modification* approach where dose is varied with location and *shape modification* approach where the size of each feature is modified. The majority of the schemes adopted the dose modification approach because it has a potential to achieve higher correction accuracy but it requires more computation. A shape modification approach has the advantage of being compatible with a wide variety of e-beam machines and also requires less storage and computation compared to dose modification.

PYRAMID [40–57], a hierarchical rule-base approach toward proximity effect correction, has been developed over years. It has been demonstrated that PYRAMID can correct circuit patterns with minimum feature size of 100 nm and below, quickly and accurately. Previous efforts in the PYRAMID project include both shape modification and dose modification for binary circuit patterns.

One of the consensus in all the previous work on e-beam proximity effect in binary lithography [16,17], analysis or correction, is that exposure variation along the resist depth dimension was not considered i.e., uses a 2-D *point spread function* (PSF) where the 2-D PSF is obtained by integrating (averaging) the corresponding 3-D PSF along the depth dimension.

Recently, there were claims of three-dimensional (3-D) proximity effect correction [21–23] for heterogeneous substrate, however, exposure variation along the resist depth dimension was not taken into account and thus still using a 2-D exposure model.

Various resist development modeling techniques, their advantages and disadvantages are described in [8–10]. Different empirical models relating the exposure and developing rate are described in [5–7]

Clear distinction between *threshold solubility* and *resist development* models, and the limitations in the threshold solubility model were described in [11].

The significance of taking resist development into account and how it affects the final resist profile were stressed in [12–15], but no correction technique was developed to reduce the non-linearity introduced by the resist development process.

1.2 Motivation and Objectives

One of the main objectives in the binary e-beam lithography is to have the resist in the circuit feature areas fully developed down to the substrate interface. The remaining resist profile depends on the 3-D spatial distribution of exposure. Also, depending on what follows the e-beam lithographic process, the desired sidewall shape of the remaining resist profile may be different. For example, undercut sidewall is needed for the lift-off process and straight vertical sidewall may be desired for anisotropic etching. Hence, there is a need for controlling the 3-D spatial exposure distribution in order to achieve the desired remaining resist profile especially for nanoscale features. Note that the depth-dependent variation of exposure becomes more noticeable as the feature size decreases. However, the 2-D proximity effect correction schemes do not consider exposure variation along the depth dimension and thus are not able to control the 3-D exposure distribution explicitly. Therefore, the main objective of this thesis is to carry out a flexibility study on true 3-D proximity effect correction via computer simulation.

The main objectives of this thesis are:

- Analysis of the 3-D proximity effect in terms of the spatial distribution of exposure in the resist through computer simulation.
- Development of the proof-of-concept 3-D proximity effect correction schemes using iso-exposure contours and remaining resist profiles.
- Performance comparison of the 3-D proximity effect correction schemes over 2-D correction techniques through computer simulation.

1.3 Organization of the Thesis

This thesis is organized as follows:

- Chapter 2 introduces the 3-D exposure and resist development models.
- Chapter 3 analyzes the 3-D proximity effect (in terms of spatial exposure distribution in the resist) considering the parameters such as beam energy, resist thickness, feature size, developing threshold, etc.
- Chapter 4 describes the proof-of-concept implementation of 3-D proximity effect correction using the iso-exposure and resist profile models.
- Chapter 5 analyzes the performance of 3-D proximity effect correction schemes over the 2-D correction scheme in terms of CD (Critical Dimension) or sidewall control.
- Chapter 6 presents conclusions and suggestions for future work.
- Appendix 1 includes some implementation issues, such as the unit of exposure and value of constants used in the resist development simulation.

CHAPTER 2

THREE-DIMENSIONAL MODELS

2.1 Electron Beam Lithography

Derived from early scanning electron microscopes, e-beam lithography uses a focused electron beam to write circuit patterns in a resist sensitive to energy deposited by electrons.

As illustrated in Figure 2.1, the features in a pattern are exposed by e-beam and a solvent developer is then used to selectively wash away the resist depending on the energy deposited in it. For a positive resist, resist is washed away if the energy deposited is higher than a certain *threshold* value ("developing threshold"). The exposure level is to be higher than the threshold within each feature and lower than the threshold in the background (unexposed area) when a positive resist is used. After the development process, the developed resist areas represent the copy of the written circuit pattern.

2.1.1 Proximity Effect Correction

Proximity effect in e-beam lithography is mainly due to the "non-ideal" distribution of exposure (energy deposited in the resist). Therefore, it is necessary to control the distribution of exposure in the resist so as to obtain the desired pattern. One of the approaches in proximity effect correction is dose modulation, wherein an optimal dose (energy incident in the resist) is searched for each region to achieve the desired exposure distribution.

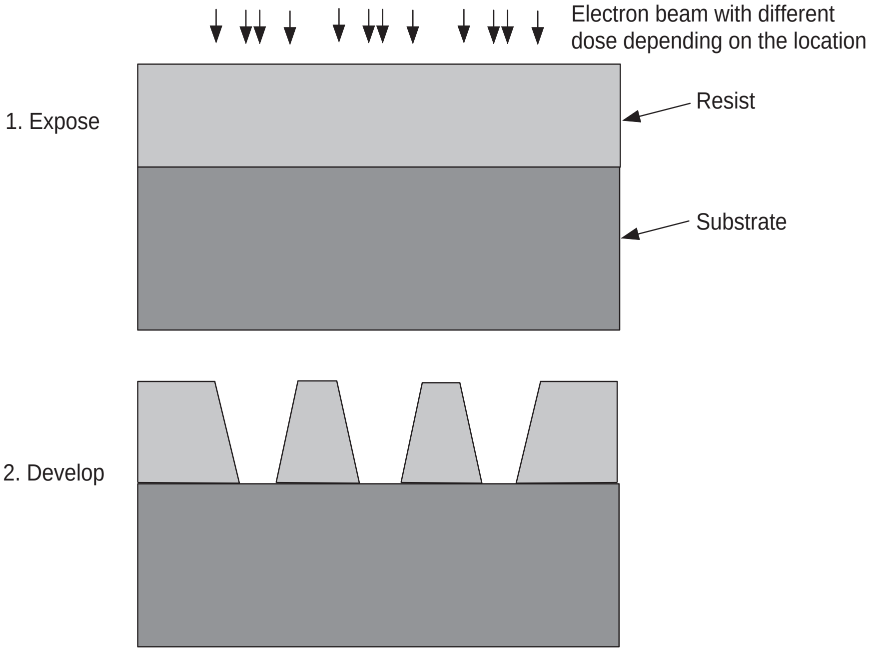

Figure 2.1: Illustration of a binary lithographic process.

2.1.2 Point Spread Function

Electron scattering can be modeled through an *energy deposition profile* or *point spread function* (PSF), which shows how the energy is distributed in the resist when a single point is exposed.

In general, the PSF is a function of the distance from the exposed point as well as depth as shown in Figure 2.2-(a). Thus, the PSF is a radially symmetric three-dimensional function. As illustrated in Figure 2.3-(a) and (b), the shape of a PSF depends on the parameters resist thickness, substrate composition, beam energy, etc., but not on the dose given to the point. For homogeneous substrates, the PSF shape does not vary with the position of the point exposed. It can also be seen from Figures 2.2-(a), 2.3-(a) and (b), that a PSF can be decomposed into two components, the *local* (or short ranged) component and the *global* (or long ranged) component [45]. The local component, due to electron's forward scattering, has large magnitude and is very sharp while the global component, due to electron's backward scattering, has relatively low magnitude and is flat.

E-beam lithographic process can be assumed to be linear and space invariant for uniform substrates. Therefore, exposing a circuit pattern can be simulated by convolving the circuit pattern with a PSF. The output of convolution represents the spatial exposure distribution.

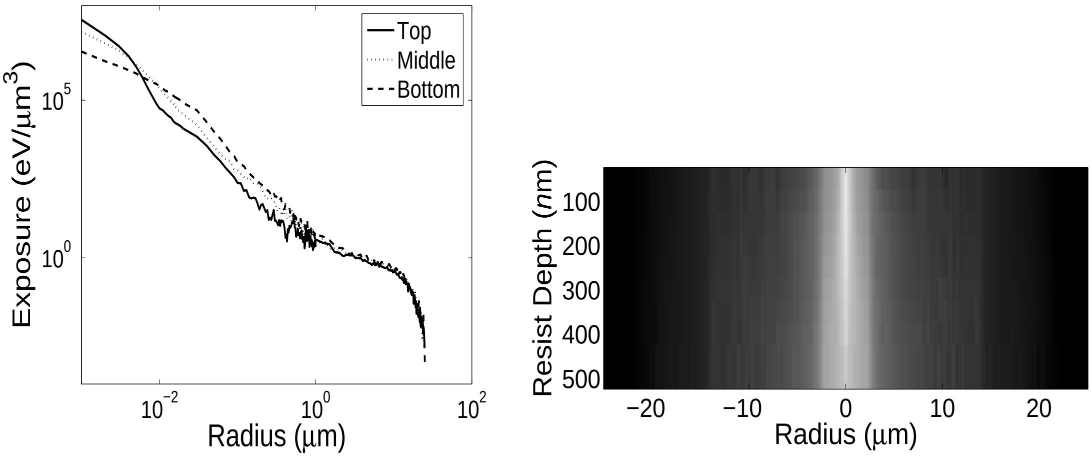

(a) (b)

Figure 2.2: A PSF for the substrate system of 500 nm PMMA on Si with the beam energy of 50 keV: (a) the top, middle and bottom layers, and (b) all layers

2.2 2-D Exposure Model

In a 2-D exposure model, variation of the exposure distribution, $e(x, y, z)$, along the Z-axis is not considered (refer to Figure 2.4 for the axes convention). A 2-D point spread function $PSF(x, y)$ is used for the computation of exposure and is obtained by averaging the 3-D point spread function $PSF(x,y,z)$ over z i.e., $PSF(x,y) = \frac{1}{T}\int_0^T PSF(x,y,z)dz$ where T is the thickness of resist. A 2-D PSF is as shown in Figure 2.3.

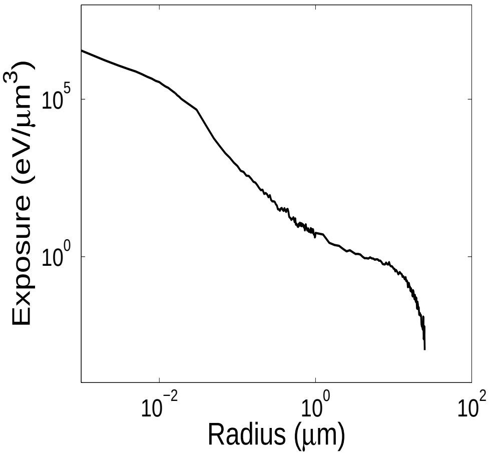

Figure 2.3: A 2-D PSF for the substrate system comprising 500 nm PMMA on Si with the beam energy of 50 keV.

Thus, 2-D exposure distribution $e(x,y)$ is given by $e(x,y) = \int_{x'}\int_{y'} PSF(x-x', y-y')f(x',y')dx'dy'$, where $f(x,y)$ represents the dose to be given to each point (x,y) on the resist surface for writing a circuit pattern. But, the actual profile of remaining resist can vary with z significantly due to the depth-dependent exposure distribution. Therefore, proximity correction using a 2-D model would not lead to an accurate result especially when a certain shape of sidewall of the remaining resist is desired.

2.3 3-D Exposure Model

In 3-D exposure model, a 3-D point spread function $PSF(x,y,z)$ is used as shown in Figure 2.2-(a) and (b), and thus the depth-dependent proximity effect is considered.

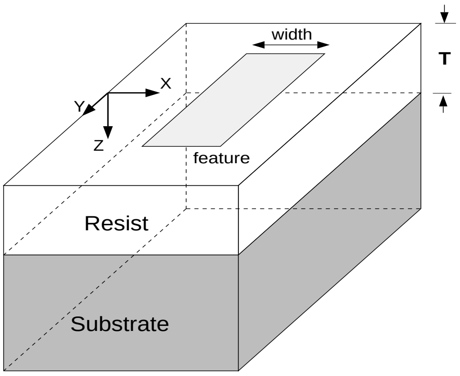

Figure 2.4: A substrate system model consisting of a substrate and resist of thickness T. Substrate system is assumed to be spatially homogeneous, i.e., the substrate composition and the resist thickness (T) do not change with location. Z-axis represents the resist depth.

As illustrated in Figure 2.2-(a) and (b), a typical PSF shows a narrow high-amplitude distribution of exposure in the top layer while a wide low-amplitude distribution in the bottom layer. This depth-dependent energy spread in the resist leads to the 3-D proximity effect which leads to variation of performance metrics with the resist depth. Since the PSF is radially symmetric about Z-axis, $PSF(x, y, z)$ may be expressed as $PSF(\sqrt{x^2 + y^2}, z) = PSF(r, z)$ where $r = \sqrt{x^2 + y^2}$.

Thus, the 3-D exposure $e(x, y, z)$ is computed using the following convolution.

$$\begin{aligned}
e(x,y,z) &= \int_{x'}\int_{y'}\int_{z'} PSF(x-x', y-y', z-z') f(x', y', 0) dx'dy'dz' \\
&= \int_{x'}\int_{y'}\int_{z'} PSF(x-x', y-y', z-z') f(x', y') \delta(z') dx'dy'dz' \\
&= \int_{x'}\int_{y'} PSF(x-x', y-y', z) f(x', y') dx'dy' \qquad (2.1)
\end{aligned}$$

From Equation 2.1, it is seen that the exposure distribution at a certain depth (z_0) can be computed by the 2-D convolution between $PSF(x, y, z_0)$ and $f(x, y, 0)$ in the corresponding plane, $z = z_0$. That is, $e(x, y, z)$ may be estimated layer by layer.

Though the 3-D exposure model provides a complete information on how electron energy is distributed in the resist, it does not directly depict the remaining resist profile after development. In order to make correction results more realistic, one has to consider the resist development process into account for correction.

2.4 Resist Development Model

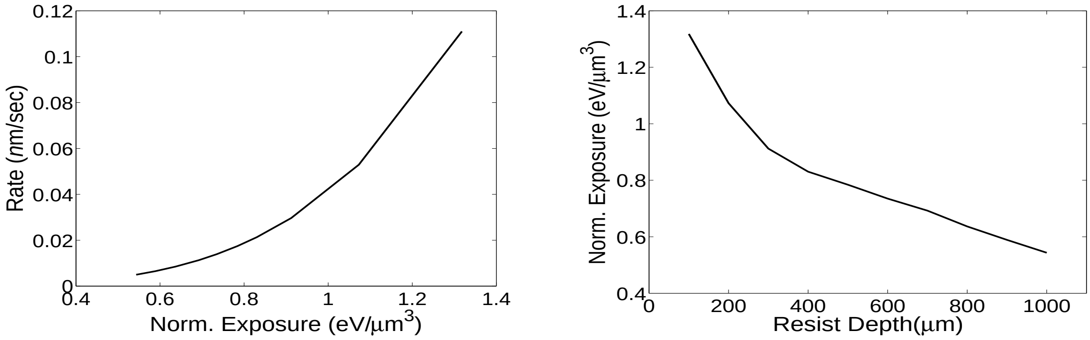

(a) (b)

Figure 2.5: Nonlinear relationship: (a) rate vs. 3-D exposure and (b) 3-D exposure vs. depth. Exposure is normalized by 10^{10}. For a feature of width L: 50 nm, Dose: 200 $\mu C/cm^2$, 1000 nm PMMA on Si, 50 keV.

Most resists are nonlinear in nature when exposed by e-beam, i.e., the resist development rate is not linearly proportional to exposure (see Figure 2.5-(a)). Exposure varies with depth z (see Figure 2.5-(b)). Also, not all points in the resist are exposed to the developer at the same time, i.e., the developing process is sequential from the top surface of resist toward the bottom. Therefore, the remaining resist profile after development can be significantly different from that estimated by the exposure models.

2.4.1 Model

To simulate the time evolution of the development profile of the resist, the exposure matrix $e(x,z)$ (eV/μm^3) is transformed into a development rate matrix $r(x,z)$ (nm/s). The relationship between r and e is determined by experimental measurements of changes in resist thickness as a function of development time for a particular resist-solvent combination. After curve-fitting such data with an analytical expression, the relationship between r and e is established.

The empirical model describing the relationship between r and e for the polymethyl methacrylate (PMMA) resist is given by Equation 2.2 [5].

$$r_{i,j} = r_0 + B(\frac{1}{\overline{M_n}} + \frac{g \cdot e_{i,j} \cdot 10^{12}}{\rho \cdot N_A})^A \tag{2.2}$$

where (i,j) is the index of cell, $\overline{M_n}$ is the original number average molecular weight, g is the chain scission per electron volt absorbed (/eV), e is the exposure (eV/μm^3), ρ is the resist polymer mass density (g/cm^3), N_A is the Avogadro's number ($= 6.023 \times 10^{23} molecules/g-mol$).

The constants r_0, A, and B are empirically determined for PMMA with different solvents (see Section A.2). Typical values for PMMA are $g = 1.9 \times 10^{-2}/eV$ (proposed by Greeneich), $\overline{M_n}$=50000, and $\rho = 1.19 g/cm^3$.

2.4.2 Simulation (Cell Removal Model)

In this thesis, a simplified version of the "cell removal algorithm" [8, 9] is implemented because it is the most robust and numerically stable of all resist development algorithms.

In the simplified cell removal algorithm, only a line feature is considered, which is long enough in the Y-dimension that any variation along Y-axis is ignored. Thus, the solubility rate and exposure matrices are functions of x and z only. The resist is divided into $m \times n$ cells in the X-Z dimension.

The reaction of developer is assumed to take place only along the normals of the cell sides. Cells are removed by the developer, one after another, according to their dissolution time dT and the number of sides in contact with the developer. When a cell is removed, the new cells exposed start developing. Any cells having an additional side exposed have their projected time of removal updated based on Equations 2.3, 2.4, and 2.5. Thus, by keeping track of the cells in contact with developer and their associated sides, the cell removal algorithm is able to simulate the development process. The result of the simulation is the development matrix, which contains the percentage development of each cell.

Thus, 2-D development algorithm as shown in Figure 2.6 involves three main steps:

- Finding the minimum dT cell and dissolving it;
- Updating the dT of other cells for the elapsed time;
- Based on the status of its neighbors, compute/recompute the time of dissolution (dT) for all undeveloped cells using Equations 2.3, 2.4, and 2.5.

Thus, the cells are removed in the order that the development proceeds.

The dissolution or development time dT of a cell is derived as follows for each condition of the cell based on its neighbors [9].

Case 1: Single side development: When a single side of a cell is exposed to a developer as shown in Figure 2.7-(a), (b), and (c), then the dissolution time dT of cell (i, j) is

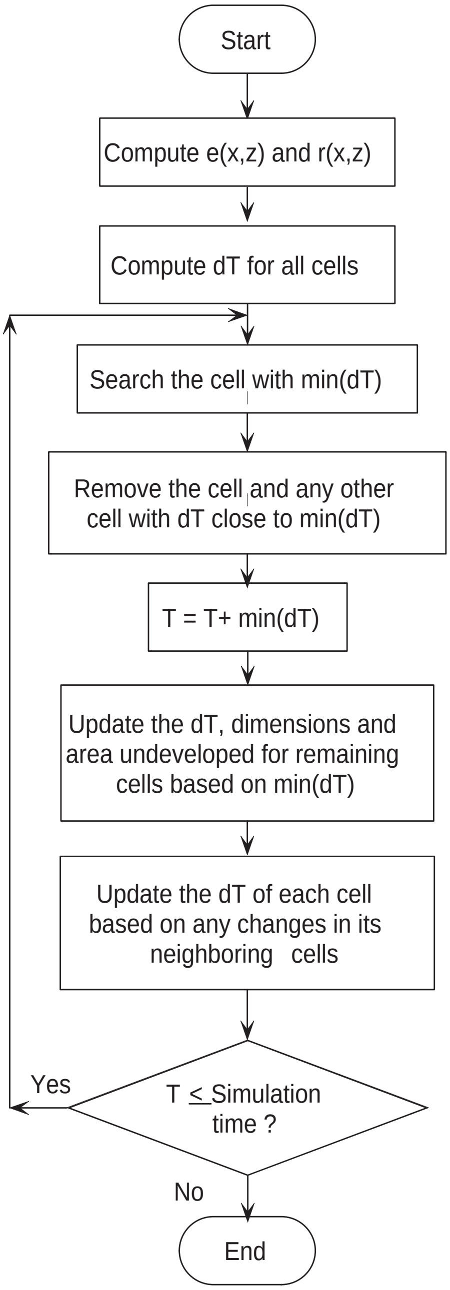

Figure 2.6: Cell removal algorithm: 2-D cell removal model.

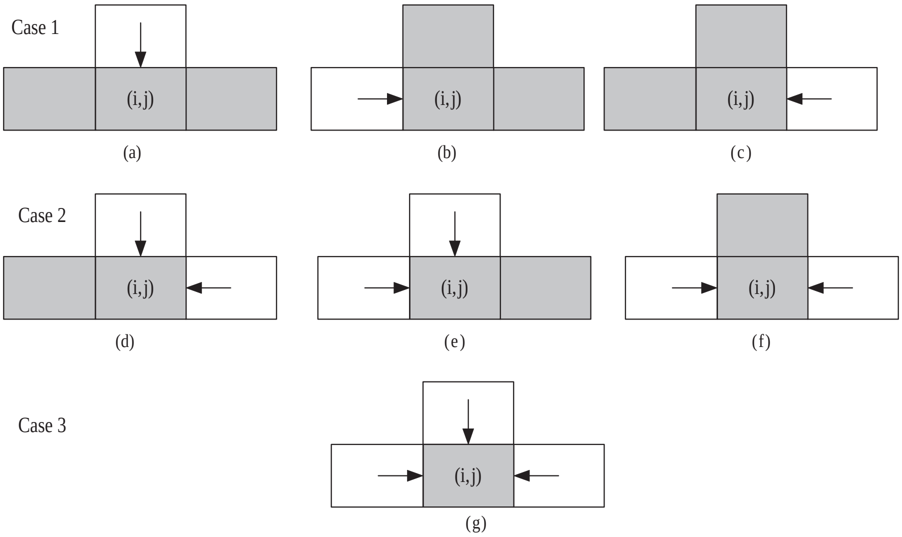

Figure 2.7: Status of cell (i, j) where Case 1: (a),(b) and (c) single side development; Case 2: (d),(e), and (f) double side development; Case 3: (g) triple side development. Unshaded are the developed cells and shaded are the undeveloped cells. Arrow heads point in the direction of developer flow.

$$dT_{i,j} = \frac{dx_{i,j} \cdot dz_{i,j}}{ds_{i,j} \cdot r_{i,j}} \tag{2.3}$$

where dx is the width, dz is the height and r is the rate of cell (i,j) and ds is the dimension dx or dz of the exposed side.

Case 2: Double side development: When two neighboring sides (for example, the dx and dz side) of a cell are exposed to the developer as shown in Figure 2.7-(d), (e), and (f), then the development time dT is accelerated for cell (i,j) as follows,

$$dT_{i,j} = \frac{dx_{i,j} \cdot dz_{i,j}}{\sqrt{dx_{i,j}^2 + dz_{i,j}^2} \cdot r_{i,j}} \tag{2.4}$$

where $\sqrt{dx_{i,j}^2 + dz_{i,j}^2}$ is the modulation factor representing the acceleration introduced by two sides exposed.

Case 3: Triple side development: When three neighboring sides (for example, the two dz and dx) of a cell (i,j) are exposed as shown in Figure 2.7-(g), then the development time dT is accelerated for cell (i,j) as follows,

$$dT_{i,j} = \frac{dx_{i,j} \cdot dz_{i,j}}{\sqrt{dx_{i,j}^2 + dz_{i,j}^2 + dz_{i,j}^2} \cdot r_{i,j}} \tag{2.5}$$

where $\sqrt{dx_{i,j}^2 + dz_{i,j}^2 + dz_{i,j}^2}$ is the modulation factor representing the acceleration introduced by three sides exposed.

In the implemented cell removal model, cells are assumed to be rectangular with default cell dimensions $dx = 5$ nm and $dz = 10$ nm where dx depends on the pixel size and dz is the distance by which the 3-D PSF is sampled along the Z-axis.

CHAPTER 3

ANALYSIS OF THREE-DIMENSIONAL PROXIMITY EFFECT IN E-BEAM LITHOGRAPHY

In this chapter, the three-dimensional (3-D) proximity effect is studied through simulation using the 3-D exposure model described in Chapter 2, when the desired sidewall is vertically straight. The effects of the parameters such as beam energy, resist thickness, feature size, developing threshold, etc. on the 3-D spatial distribution of exposure in the resist, in particular, depth-dependent proximity effect, are considered in the analysis. The remaining resist profile after development is mainly determined by the spatial distribution of exposure though the development process can also affect the profile which is studied in detail in Chapters 4 and 5.

3.1 Intra-Proximity Effect

The intra-proximity effect refers to the proximity effect within a feature. In order to quantify the 3-D intra-proximity effect, the two metrics, *width variation* and *exposure contrast*, are introduced.

Width Variation

The width of a line feature may vary with the resist depth after development as illustrated in Figure 3.1. The line feature is long enough in the Y direction that its width can be assumed not to vary with y. Let $W(z)$ denote the width of the line feature where z is the depth in the resist. In this simulation study, it is assumed that $W(z)$ can be approximated by the *iso-exposure contour* determined by $e(x, z) = Thr$ where Thr is the developing threshold (refer to Figure 3.4-(b)). Note that $e(x, y, z)$ does not vary with y in the middle of the line. Let W_t and W_b represent the widths of the line at the top and bottom layers of resist, respectively, i.e., $W_t = W(0)$ and $W_b = W(T)$ where T is the thickness of resist. Also, the average width, w, of the line is defined to be $\frac{1}{T}\int_0^T W(z)dz$. *Width variation*, δ_w, quantifies deviation from the straight vertical sidewall, and is defined to be $\frac{W_t - W_b}{W}$. Note that $\delta_w > 0$ and $\delta_w < 0$ indicate *overcut* and *undercut*, respectively. When the sidewalls are vertically straight, $\delta_w = 0$. That is, the measure of δ_w can not only quantify the width variation, but also indicate the type of sidewall.

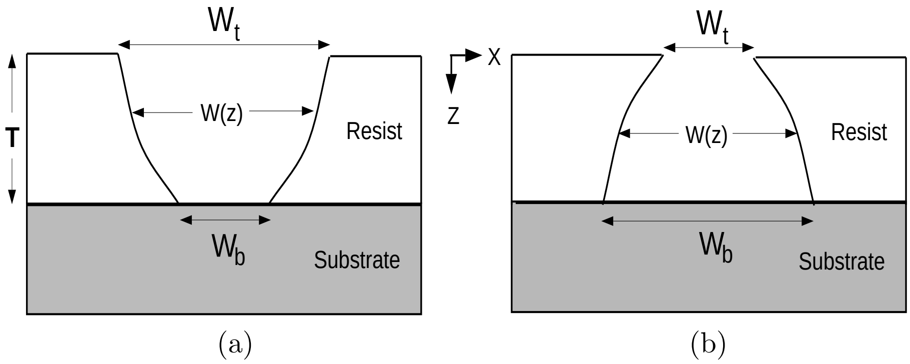

Figure 3.1: Cross-section of the remaining resist for a line feature: (a) overcut ($\delta_w > 0$) and (b) undercut ($\delta_w < 0$).

Exposure Contrast

For a long line feature along the Y axis, *exposure contrast* (or *gradient*), $C(z)$, is defined as $|\frac{\partial e(x,y,z)}{\partial x}|_{e=Thr}|$. Given a developing threshold Thr, the iso-exposure contour of $e(x, z) = Thr$ is determined on the X-Z plane. Then, $C(z)$ is computed across the iso-exposure contour, i.e., it quantifies how fast the exposure changes spatially around the developing threshold. The exposure contrast needs to be higher for a smaller variation of the feature dimension due to the varying development process. The exposure contrast varies with the resist depth.

3.2 Inter-Proximity Effect

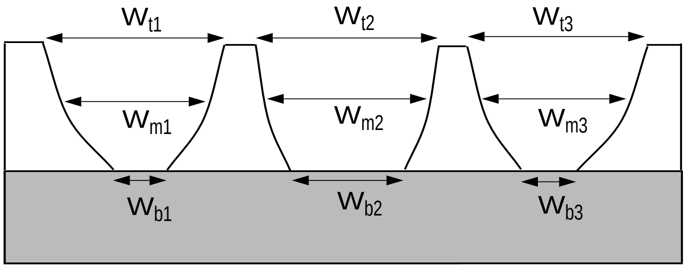

Figure 3.2: Variation of line width due to inter-proximity effect among multiple lines when $\delta_{wi} > 0$ for all i.

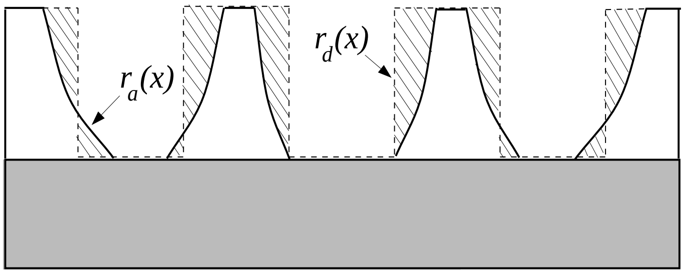

Figure 3.3: Comparison of the remaining resist profile ($r_a(x)$) with the desired one ($r_d(x)$ of "straight vertical sidewalls") where the difference between the two profiles is shown as the shaded areas. The ratio of line to space (L:S) is 1:1.

When multiple features are close to each other, the interaction among them leads to the *inter*-proximity effect [25]. The level of inter-proximity effect varies with depth in the resist since the exposure distribution, $e(x, y, z)$, is a function of the resist depth, z. This 3-D inter-proximity effect makes the line width vary spatially and the amount of variation depends on the resist depth. As one way to quantify the 3-D inter-proximity effect, the spatial variation of line width among lines is considered for a uniform typical line-space pattern. Let W_{ti}, W_{mi} and W_{bi} denote the widths of the ith line at the top, middle, and bottom layers, respectively, as illustrated in Figure 3.2. Then, for the top layer, the normalized standard deviation of W_{ti} is computed as $\sigma_{w_t} = \frac{1}{\overline{W}_t}\sqrt{\frac{1}{N}\sum_{i=1}^{N}(W_{ti} - \overline{W}_t)^2}$ where $\overline{W}_t$ is the mean of W_{ti} among the lines, i.e., $\overline{W}_t = \frac{1}{N}\sum_{i=1}^{N} W_{ti}$ and N is the number of lines. Similarly, for the middle and bottom layers, σ_{w_m} and σ_{w_b} may be computed from $\{W_{mi}\}$ and $\{W_{bi}\}$, respectively. For a non-uniform pattern, e.g., the line width varies with line, W_{ti} (W_{mi}, W_{bi}) may be normalized by the average width of the ith line, $w_i = \frac{1}{T}\int_0^T W_i(z)dz$, before σ_w is computed. Note that this measure (σ_w) of inter-proximity effect only quantifies how uniform the remaining resist profile is among multiple features. It does not directly indicate the deviation from a desired profile.

When a desired profile is known, a quantitative measure of difference between the desired and actual profiles can be defined to supplement the measure of σ_w. Let $r_d(x)$ and $r_a(x)$ depict the desired and actual profiles, respectively, as illustrated in Figure 3.3. Note that $r_a(x)$ is the iso-exposure contour of $e(x, z) = Thr$. Then, the difference (or error) measure may be computed as $\epsilon = \frac{1}{XT}\int_0^X |r_a(x) - r_d(x)|dx$ where X is the width of a pattern (e.g., for 3 lines of width L, and 3 spaces of width S, $X = 3(L + S)$).

3.3 Simulation Results and Discussion

The simulation model employed in this study takes only exposure into account. 3-D exposure distribution in the resist is computed by the layer-by-layer 2-D convolution which is accelerated by the CDF (Cumulative Distribution Function) table method [45]. Changing the base dose (“dose” hereafter), i.e., changing the dose distribution uniformly, simply scales the exposure distribution. Hence, analyzing effects of different doses may be carried out by considering different developing thresholds for the same exposure distribution. This eliminates the need to repeat the same convolution with different scaling factors in the simulation. In all cases, exposure was computed at 10 layers of resist, which are equally spaced.

3.3.1 Iso-Exposure Contours

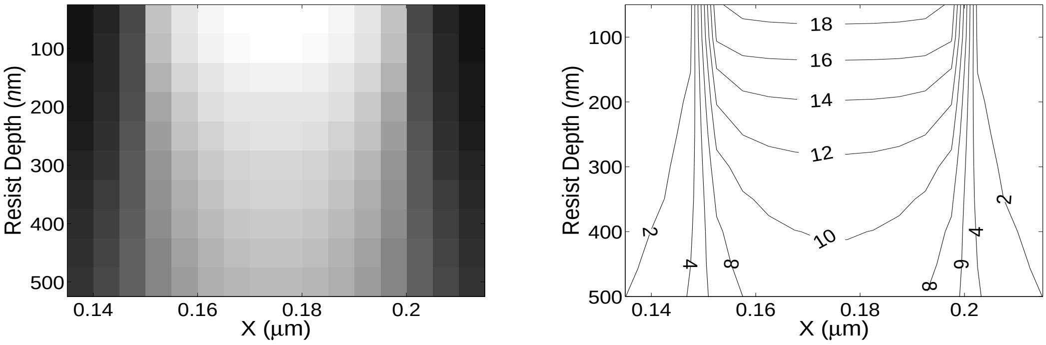

(a) (b)

Figure 3.4: Cross-sections (X-Z plane) of exposure distribution in the resist when a rectangular feature with the width (L) of 50 nm is exposed with the dose of 200 $\mu C/cm^2$: (a) grayscale image and (b) iso-exposure contours. The substrate system consists of 500 nm PMMA on Si and the electron beam energy is 50 keV. The unit of exposure is $\mu C/cm^2$.

In Figure 3.4, the cross-section $e(x, z)$ of spatial exposure distribution is shown for a rectangular circuit feature when the dose is 200 $\mu C/cm^2$ (refer to Figure 2.4). It can be seen that the exposure distribution varies with the resist depth. The iso-exposure contour plot in Figure 3.4-(b) indicates that the remaining resist profile can be quite different depending on the dose or developing threshold. Suppose that the developing threshold is 8 $\mu C/cm^2$. Then, in order to achieve the vertical sidewalls, the dose needs to be doubled (to 400 $\mu C/cm^2$). Note that the contour of 4 $\mu C/cm^2$ is almost vertical in Figure 3.4-(b). In addition to the line width variation, one can also see the dependency of exposure contrast on the resist depth, i.e., higher at the top layer than at the bottom layer. In Figure 3.5, dependency of the line width on the resist depth is shown for two different thicknesses of resist. The line width varies significantly with the resist depth and the variation is larger for a thicker resist.

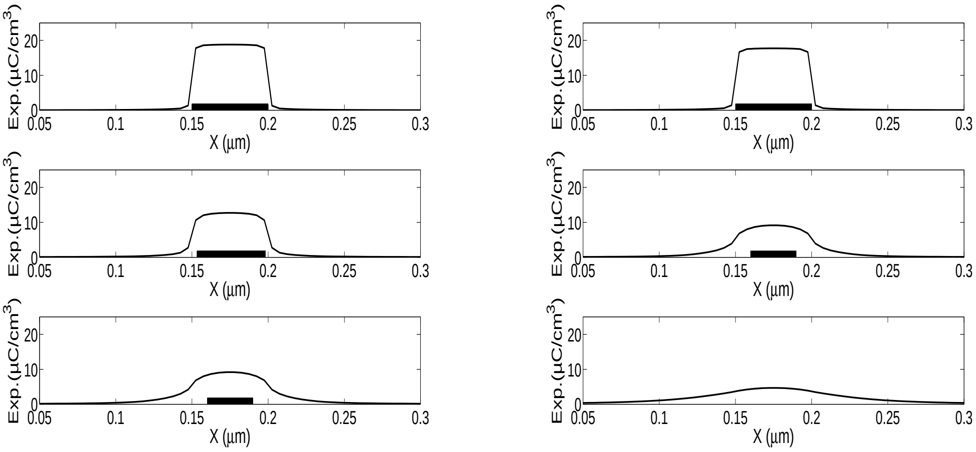

(a)

(b)

Figure 3.5: Dependency of line width (after development) on resist depth (top, middle and bottom layers) for the substrate system of PMMA on Si and 50 keV with the dose of 200 $\mu C/cm^2$: (a) 500 nm PMMA and (b) 1000 nm PMMA. The developing threshold is 8 $\mu C/cm^2$.

3.3.2 Intra-Proximity Effect

Resist Thickness

In Figure 3.6, iso-exposure contours are plotted for two different thicknesses of resist. When the resist is 100 nm thick, the contours show little variation along the depth dimension (refer to Figure 3.6-(a)), i.e., not much 3-D proximity effect. However, as the resist thickness

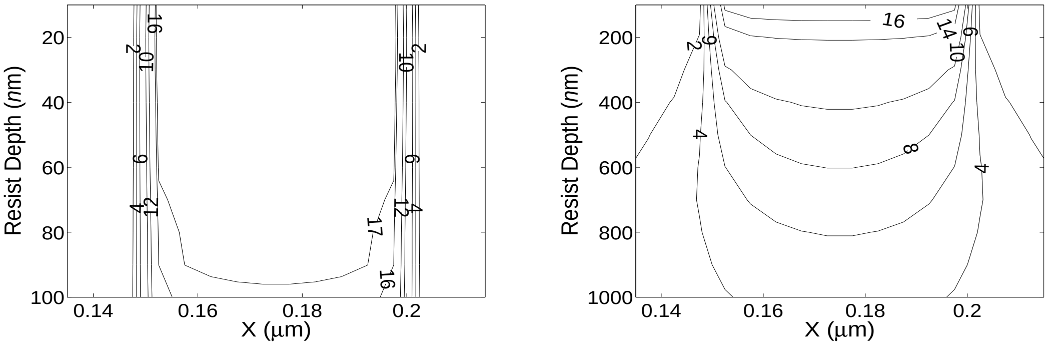

(a)

(b)

Figure 3.6: Dependency of iso-exposure contours on the resist thickness: (a) 100 nm PMMA on Si and (b) 1000 nm PMMA on Si. The unit of exposure is $\mu C/cm^2$. L: 50 nm, dose: 200 $\mu C/cm^2$, 50 keV.

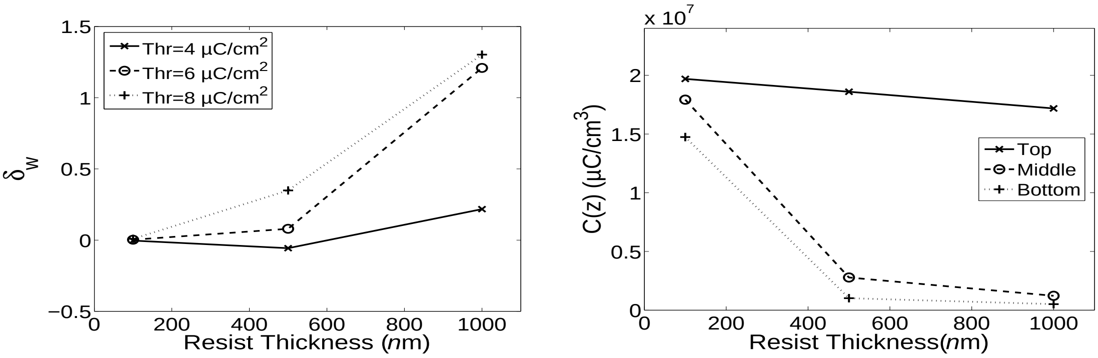

(a)

(b)

Figure 3.7: Dependency of δ_w and C on the resist (PMMA) thickness: (a) δ_w and (b) C ($Thr = 2\mu C/cm^2$). L: 50 nm, dose: 200 $\mu C/cm^2$, 50 keV.

increases, the 3-D proximity effect becomes larger, leading to a significant depth-dependent variation in exposure distribution as shown in Figure 3.6-(b) where the resist thickness is 1000 nm. In Figure 3.7, the line width variation (δ_w) and exposure contrast (C) are analyzed by varying the resist thickness. As the resist thickness increases, δ_w becomes larger as expected (Figure 3.7-(a)). It is also seen that δ_w is larger for a higher (developing) threshold (equivalently a lower dose for a fixed threshold). In Figure 3.7-(b), it is observed that C decreases as the resist thickness increases since the electron energy spreads more for a thicker resist. The decrease in the exposure contrast is more evident in the lower layers.

Beam Energy

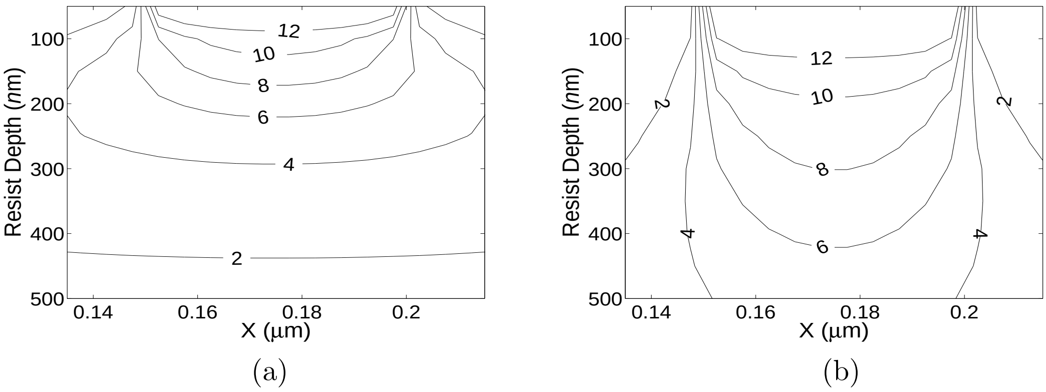

(a)

(b)

Figure 3.8: Dependency of iso-exposure contours on the beam energy: (a) 5 keV and (b) 20 keV. The unit of exposure is $\mu C/cm^2$. Dose: 200 $\mu C/cm^2$, L: 50 nm, 500 nm PMMA on Si.

Dependency of the iso-exposure contours on the beam energy is shown in Figure 3.8 (also refer to Figure 3.4-(b)). As the beam energy increases, electrons can penetrate deeper into the resist leading to a more vertical orientation of the contours, which makes δ_w smaller.

However, the beam energy higher than a certain value may be lead to an undercut due to excessive backscattering from the substrate depending on the resist thickness.

Feature Size

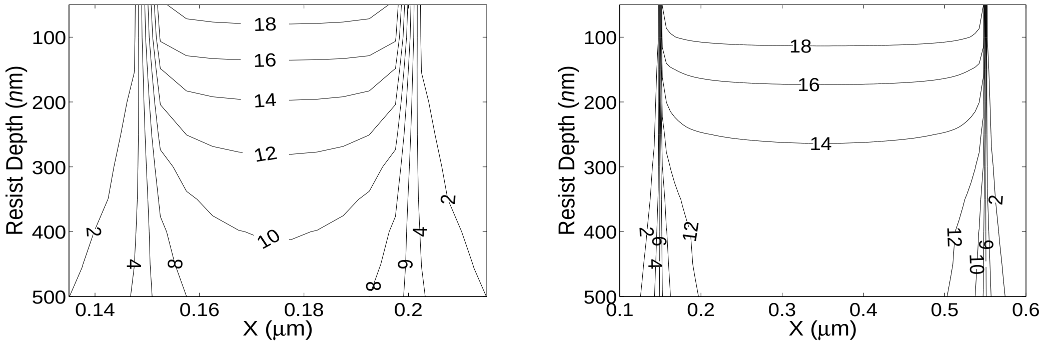

(a) (b)

Figure 3.9: Dependency of iso-exposure contours on feature size (L: line width): (a) $L =$ 50 nm and (b) $L = 400$ nm. The unit of exposure is $\mu C/cm^2$. Dose: 200 $\mu C/cm^2$, 500 nm PMMA on Si, 50 keV.

In Figure 3.9, iso-exposure contours are compared for two different feature sizes (line widths). When the feature size is small as in Figures 3.9-(a), the exposure variation along the depth dimension is significant. However, for large features, the variation is relatively small as can be seen in Figure 3.9-(b). Note that the exposure difference between the top and bottom layers is about 10 and 6 $\mu C/cm^2$ for the small and large features, respectively.

Threshold

As mentioned earlier, increasing (or decreasing) the dose with a fixed developing threshold is equivalent to decreasing (or increasing) the threshold with a fixed dose. In Figure 3.10, effects of the threshold (dose) on δ_w and C are analyzed. For a higher threshold (a lower dose), δ_w is larger, i.e., the line width varies more with the resist depth as shown in Figure 3.10-(a). Also, the remaining resist profile tends to be overcut ($\delta_w > 0$). As the threshold decreases (the dose increases), δ_w decreases. Particularly for a high beam energy, δ_w can become negative, i.e., the remaining resist profile of undercut. The exposure contrast, C, is shown in Figure 3.10-(b). It is seen that the exposure contrast is highest at the top layer, and decreases as the resist depth increases. In a layer, as the threshold increases, C shows a bitonic behavior, i.e., an increasing interval followed by a decreasing interval. This is due to the typical characteristics of spatial exposure distribution over the feature edges (refer to Figure 3.5 noting that C is an exposure gradient).

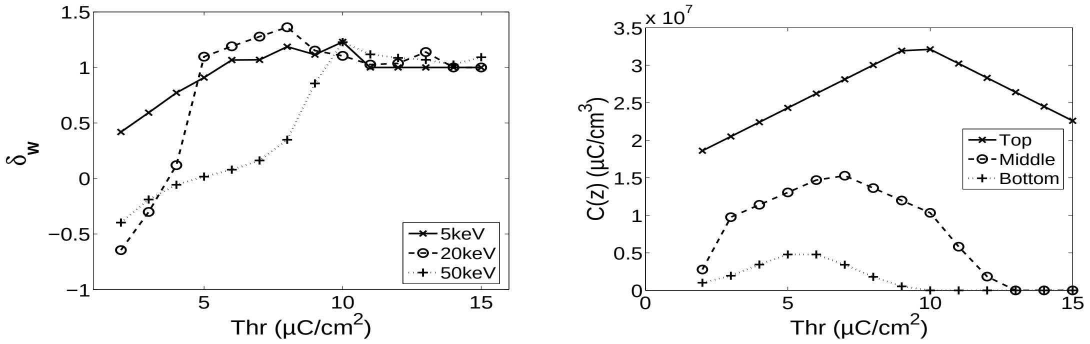

(a) (b)

Figure 3.10: Dependency of δ_w and C on threshold or equivalently dose: (a) δ_w and (b) C (exposure contrast). Dose: 200 $\mu C/cm^2$, L: 50 nm, 500 nm PMMA on Si, 50 keV.

3.3.3 Inter-Proximity Effect

Variation of Line Width and Exposure Contrast

As shown in Figure 3.11, the width variation (σ_w) among the (three) lines due to inter-proximity effect is largest at the bottom layer and least at the top layer. This is due to the fact that energy spread due to electron scattering is greater at a lower layer of resist. Also, as the resist thickness increases or the beam energy decreases, σ_w increases significantly

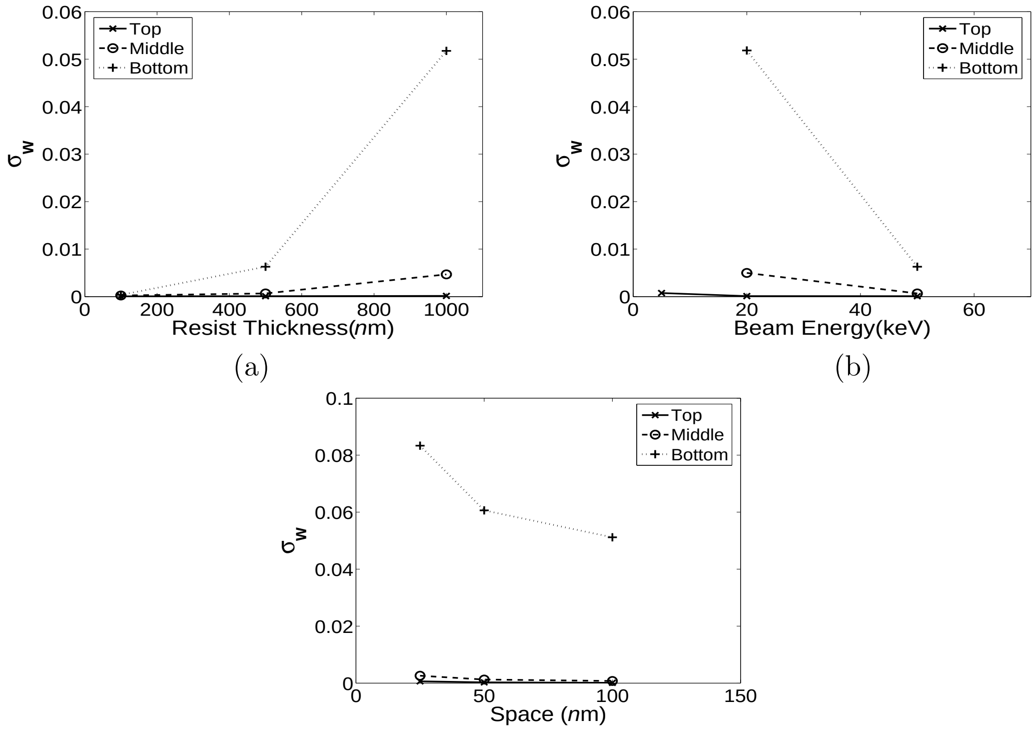

(a) (b)

(c)

Figure 3.11: Dependency of σ_w on (a) resist thickness, (b) beam energy (S=100nm, $Thr = 4\mu C/cm^2$, $T = 500$ nm), and (c) S ($Thr = 9\mu C/cm^2$, $T = 500$ nm). Dose: 200 $\mu C/cm^2$, L: 50 nm, 50 keV, PMMA on Si.

except for the top layer where the exposure contrast is highest. In particular, as the space (S) between lines decreases, the inter-proximity effect increases, which makes σ_w larger. The increase is greater at the bottom layer (than at the top layer). Also, it is observed that the exposure contrast (C) has a larger deviation among the lines for a lower layer, a thicker resist, and a smaller line spacing.

Error in Resist Profile

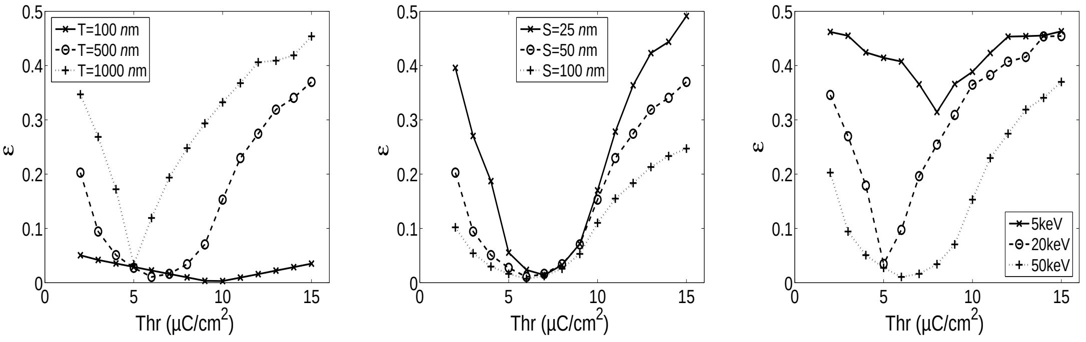

(a) (b) (c)

Figure 3.12: Dependency of ϵ on (a) resist thickness (50 keV), (b) S (50 keV), and (c) beam energy. Dose: 200 $\mu C/cm^2$, L: 50 nm, 500 nm PMMA on Si, $Thr : 4\mu C/cm^2$.

In Figure 3.12, the error, ϵ, between the desired and actual remaining resist profiles is analyzed when the desired profile has straight vertical walls. It is observed that there exists a threshold (equivalently a dose) which minimizes the error. As expected, the error is larger for a thicker resist as shown in Figure 3.12-(a). As the (three) lines get closer, i.e., the space, S, between lines decreases, a higher level of inter-proximity effect is incurred leading to a larger error. Low-energy electrons cannot penetrate deep into the resist. Hence, the minimum ϵ one can achieve by controlling the dose is significantly larger for a lower beam energy than a higher beam energy as seen in Figure 3.12-(c).

Undercut/Overcut

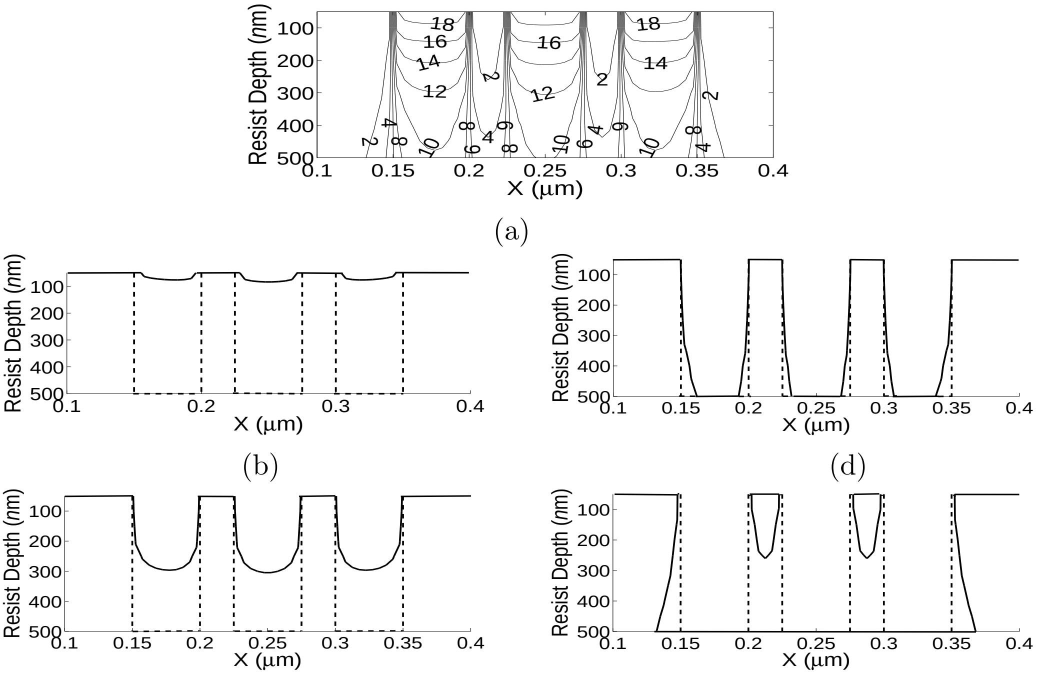

(a)

(b)

(d)

(c)

(e)

Figure 3.13: Dependency of the remaining resist profile on developing threshold: (a) exposure contours, (b) $Thr = 18\ \mu C/cm^2$, (c) $Thr = 12\ \mu C/cm^2$, (d) $Thr = 9\ \mu C/cm^2$, and (e) $Thr = 2\ \mu C/cm^2$. Dose: 200 $\mu C/cm^2$, L: 50 nm, S: 25 nm, 500 nm PMMA on Si, 50 keV. The dashed lines show the ideal line widths.

In Figures 3.13 and 3.14, the profile of remaining resist is examined by changing the threshold (dose) or line spacing. It is illustrated that the inter-proximity effect becomes visible when the dose is increased or the space between lines is decreased. Also, it is to be noted that the inter-proximity effect is layer-dependent and is most severe at the bottom layer. As the dose is increased (i.e., the threshold is decreased), the level of inter-proximity effect increases especially at the lower layers and eventually the three lines are merged due to the undercut at the lower layers while still separated at the upper layers as shown in

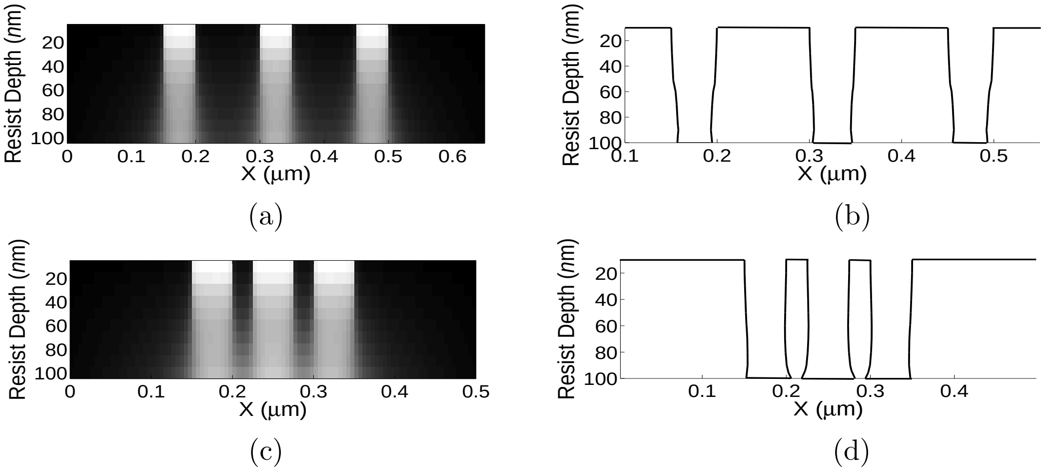

Figure 3.14: Dependency of the remaining resist profile on line spacing (S): (a) & (b) $S = 100$ nm and (c) & (d) $S = 25$ nm. Dose: 200 $\mu C/cm^2$, $Thr = 10$ $\mu C/cm^2$, L: 50 nm, 100 nm PMMA on Si, 5 keV.

Figure 3.13. Similar observations can be made when the lines get closer to each other as shown in Figure 3.14.

2-D vs. 3-D

In the simulation where a 2-D model is employed, any variation (of exposure) along the depth dimension (Z) is not taken into consideration or assumed to be zero. Therefore, equivalently, the remaining resist profile is completely vertical i.e. the equivalent 3-D exposure $e(x, z)$ is obtained from 2-D exposure $e(x)$ by replicating the 2-D exposure values $e(x)$ along the depth of the resist.

3.3.4 Exposure

In Figure 3.15, the 2-D (dashed lines) and 3-D (solid lines) models are compared in terms of the remaining resist profile. In Figure 3.15-(a) where $S = 100$ nm and the threshold is 7 $\mu C/cm^2$, the 2-D model estimates the line width to be about 35 nm. However, the profile estimated by the 3-D model shows that the line width is wider (than that estimated by the 2-D model) in the top half of the resist layers and then becomes narrower, i.e., an overcut. Also, the bottom one third of resist layers is not even developed. When the threshold is lowered (or the dose is increased), overcuts may become undercuts and wider line widths may result at lower layers in the 3-D model as shown in Figure 3.15-(b). Also, it should be noticed that the center line is wider than the other two "end lines" at the bottom of resist. In addition, the centers of the end lines are shifted toward the center line more at the bottom of resist than at the top. For an even lower threshold as in Figure 3.15-(c), the lines are merged at the lower layers according to the 3-D model while they are well separated in the 2-D profile. When S = 25 nm, the inter-proximity effect is greater, however, similar observations can be made as shown in Figures 3.15-(d), (e) and (f). In Figure 3.15-(f), the 2-D model indicates that all three lines are completely merged while the 3-D model shows some undeveloped resist between the lines except at few lower layers. It is clear that the 2-D and 3-D models lead to significantly different estimation results. In particular, the 2-D model is not able to distinguish the overcut and undercut from the vertical straight wall.

3.3.5 Resist Development Profile

Shown in Figure 3.16-(a) and (b) are the 2-D exposure distribution and its corresponding development contours. It is seen that 2-D model fails to depict the intra-proximity effect in the feature and thus inaccurately predicts the remaining resist profiles. Also, shown in Figure 3.16-(c) and (d) are the 3-D exposure distribution and its development contours.

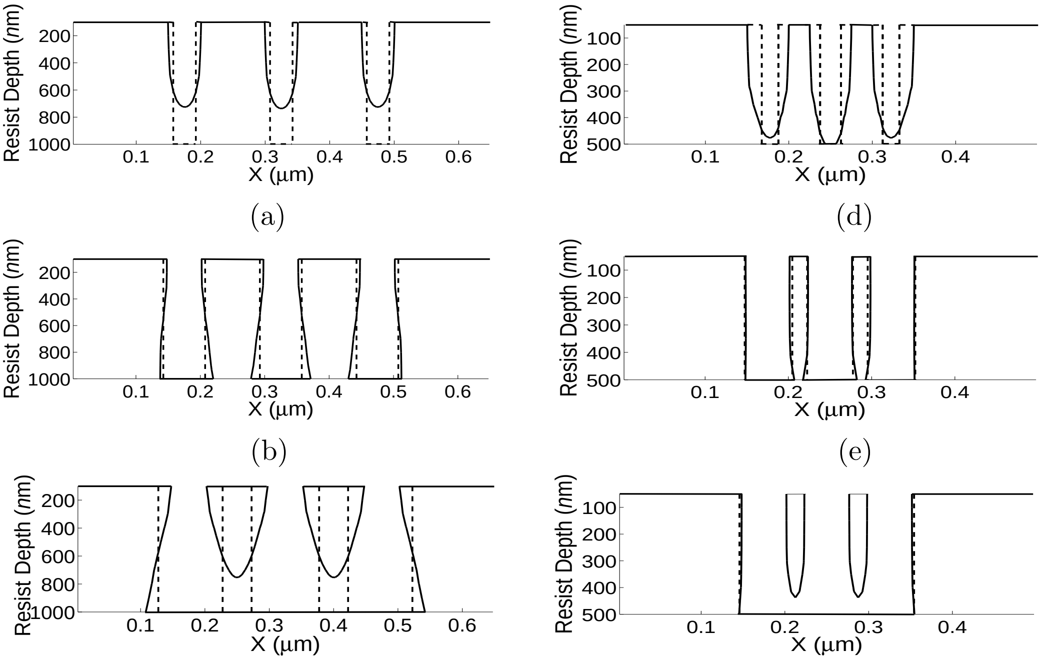

(a) (d)

(b) (e)

(c) (f)

Figure 3.15: Comparison of remaining resist profiles between 2-D (dashed) and 3-D (solid) models using iso-exposure contours. For S: 100 nm (1000 nm PMMA on Si), (a) $Thr = 7\mu C/cm^2$, (b) $Thr = 3\mu C/cm^2$ and (c) $Thr = 1.5\mu C/cm^2$. For S: 25 nm (500 nm PMMA on Si), (d) $Thr = 10\mu C/cm^2$, (e) $Thr = 5\mu C/cm^2$ and (f) $Thr = 4\mu C/cm^2$. Dose: 200 $\mu C/cm^2$, L: 50 nm, 50 keV.

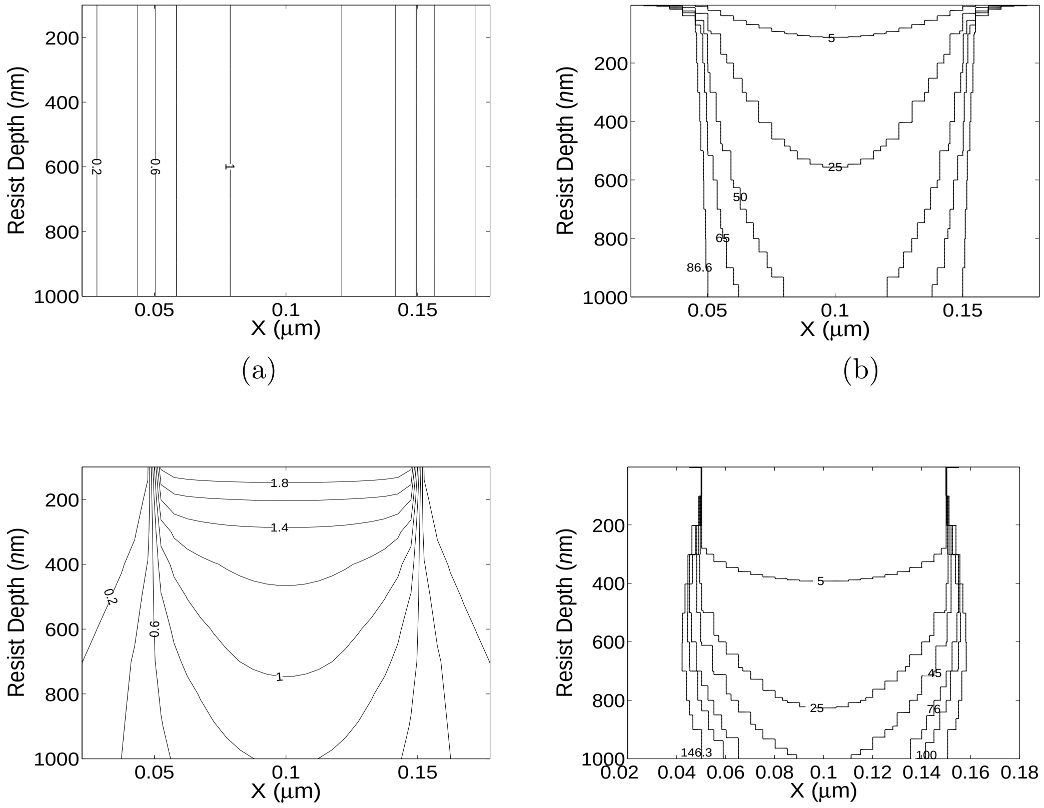

(a) (b)

(c) (d)

Figure 3.16: Comparison of remaining resist profiles between 2-D ((a) and (b)) and 3-D models ((c) and (d)) using resist development contours for different development times (*min*). (a) 2-D iso-exposure and (b) development contours using 2-D PSF, (c) 3-D iso-exposure and (d) development contours using 3-D PSF for a rectangular feature of width (L):100 nm, Dose: 300 $\mu C/cm^2$, 1000 nm PMMA on Si, 50 keV. The unit of exposure is eV/μm^3 normalized by 10^{10}.

It is seen that no remaining resist profile (development contour) matches any iso-exposure contour. Also, it is observed that the shape of remaining resist profile depends on the development time. Therefore, in order to develop an accurate 3-D correction scheme, one needs to consider the remaining resist profile instead of exposure contours.

CHAPTER 4

THREE-DIMENSIONAL CORRECTION APPROACHES

In this chapter, 3-D correction methods which use a 3-D exposure model in controlling the e-beam dose distribution within each circuit feature to achieve the desired sidewall profile are described.

The following two proof-of-concept implementations of 3-D proximity effect correction for binary circuits, developed based on PYRAMID [45, 52–55, 57], are presented:

- 3-D iso-exposure contour correction (pre-development exposure contour)
- 3-D resist profile correction (post-development resist contour)

The prototype versions consider the exposure only along the cross-section of line patterns for correction, under the assumption that the feature is sufficiently long along the Y-dimension.

4.1 PYRAMID Correction Procedure

Figure 4.1 shows the basic correction procedure of the binary PYRAMID. First, a circuit pattern is loaded from an input file. The input file includes a set of rectangles that represent the boundaries of features. In the *rectangle partitioning* step, an input rectangle may be partitioned into smaller rectangles if necessary. A rectangle is further partitioned into multiple regions in the *region partitioning* step. A region is the smallest spatial unit in controlling dose. Within each region, dose is constant and equal to the product of dose factor and the base dose. In binary circuits, a rectangle is partitioned into center and

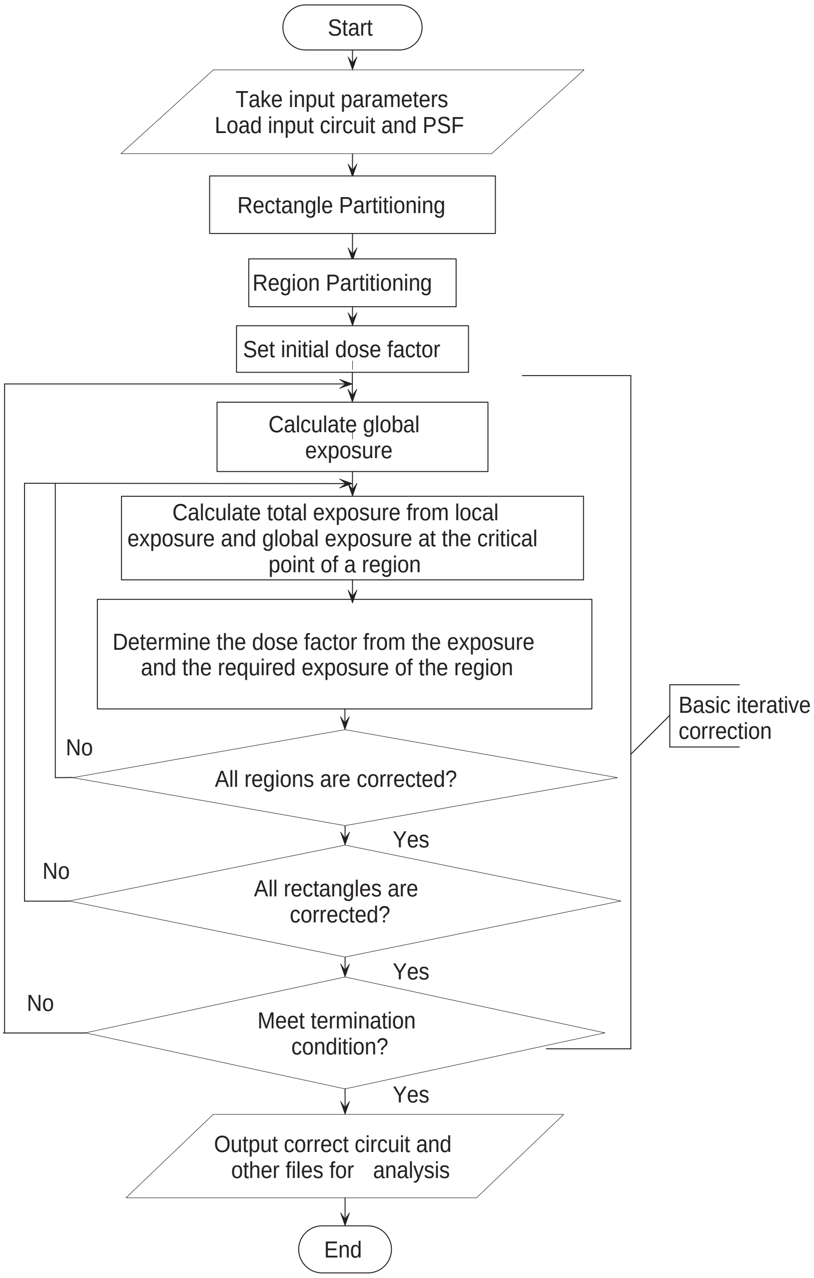

Figure 4.1: The basic correction procedure of dose modification PYRAMID for binary circuit patterns.

boundary regions. The center region's exposure is targeted for a minimum exposure of $ThrC$, while for boundary regions, it is targeted for $ThrB$, where $ThrB < ThrC$. Each region contains a *critical point.* Critical points serve as the control points in the PYRAMID approach, where accuracy of the correction result is evaluated.

After setting the initial dose factor for every region, an iterative nonrecursive correction is performed for the entire circuit as shown in Equation 4.1.

$$D_{adj} = \begin{cases} F_{adj} \cdot (D_{tmp} - D_{old}) + D_{old} & \text{if } D_{adj} \geq 0 \\ 0 & \text{if } D_{adj} < 0 \end{cases} \tag{4.1}$$

where D_{old} is the dose factor in the previous iteration, D_{tmp} is the dose factor computed in the current iteration, F_{adj} is the adjustment factor, and D_{adj} is the new adjusted dose factor for the region.

In each iteration, all regions are corrected by the dose modification algorithm shown in Figure 4.2. The adjusted dose factor for each region is computed such that the CD error at the critical point(s) is minimized. The iteration continues until a certain termination condition is met. The termination condition could be a certain number of iterations completed, having found an acceptable solution or that the correction procedure cannot further improve the solution.

4.2 3-D Iso-Exposure Contour Correction

Developed from the previous dose modification PYRAMID for binary correction, the 3-D iso-exposure contour correction adopts an iso-exposure contour to fit to the desired remaining resist profile. The exposure estimation is modified along with the location of

```
For each iteration:
 For each rectangle:
  Find the Exposure $E_c$ at the center region $R_c$;
     Set dose $D_c$ of $R_c$ such that $E_c$ is at least $ThrC$
     where $ThrC$ is the desired exposure for the center region;
  For each other region $R_i$ where $i$=1 to $n$:
     Find exposure $E_i$ at the boundary location;
     Set dose $D_i$ of $R_i$ such that $E_i$=$ThrB$
     where $ThrB$ (< $ThrC$) is the development threshold;
```

Figure 4.2: Dose modification algorithm for binary lithography. All the resist above the developing threshold $ThrB$ gets dissolved off by proper selection of solvent.

critical points and dose calculation. Each region is corrected using the 3-D exposure model described in Section 2.3. The goal of the 3-D correction scheme is to match an iso-exposure contour to the shape of the sidewall that needs to be achieved.

In binary circuits, three kinds of sidewalls are possible, namely, undercut, vertical, and overcut. Critical points are located in the 3-D space and their locations depend on the shape of the sidewall as shown in Figure 4.3. Two critical points are chosen, as in the earlier version of PYRAMID, one inside ($InLcn$) and the other outside ($OutLcn$) the desired sidewall of the feature. For vertical sidewall, the horizontal location of critical point in a resist layer does not change with layer as shown in Figure 4.3-(b). For undercut, the critical points are shifted out with reference to the feature boundary by a larger amount for a lower layer as shown in Figure 4.3-(a) while for overcut, the critical points are shifted in with reference to the feature boundary by a smaller amount for a lower layer as shown in Figure 4.3-(c).

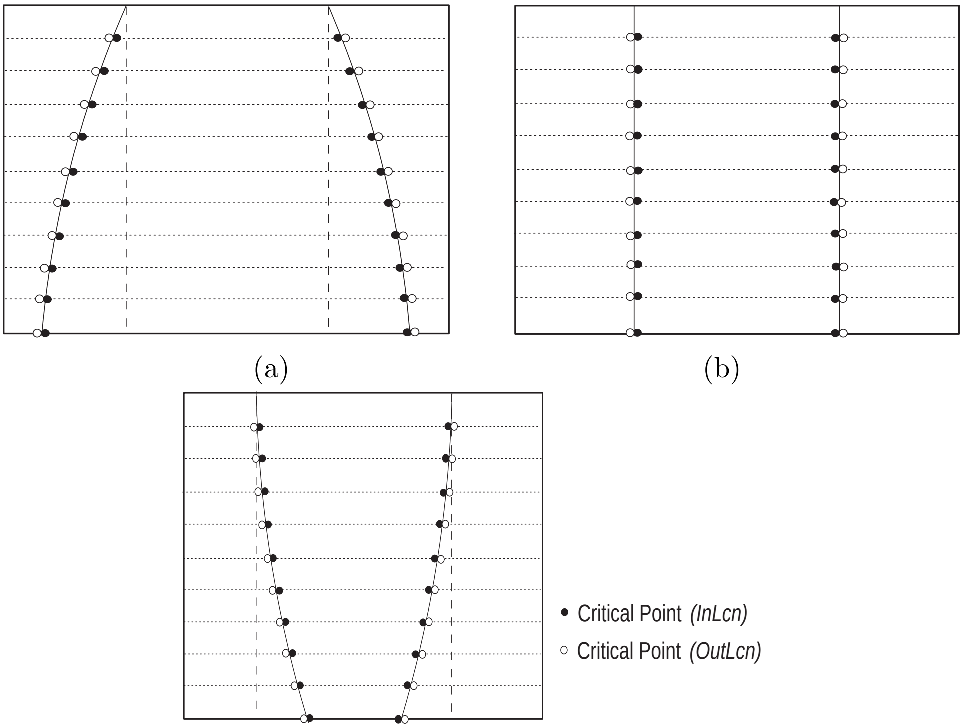

(a) (b)

(c)

Figure 4.3: Cut-view ($X - Z$) of a feature to show sidewall shape and its corresponding critical points setup: (a) Undercut, (b) Vertical, and (c) Overcut. Two critical points are used, one inside (*InLcn*) and the other outside (*OutLcn*) the desired sidewall. Dotted lines are the PSF layers, dashed lines are the feature boundaries, and bold continuous lines are the desired sidewall boundaries.

In the current implementation, an iterative optimization approach is adopted where the *cost function* to be *minimized* is given by Equation 4.2,

$$Costfunction(df) = \sum_{i=0}^{9} (E_R(z_i) - E_{iso}(z)) \tag{4.2}$$

where depth index i varying from 0 to 9, $E_R(z_i)$ is the exposure computed at the critical point for a region at depth z_i, and $E_{iso}(z)$ is the iso-exposure.

Figure 4.4 shows the optimization approach to determine the optimal dose factor that minimizes the exposure error. Only the top, middle and bottom PSF layers are used in order to save computation time and memory. Accuracy will improve if all the PSF layers are used for correction.

After setting the initial dose factor for each region, the iterative correction is performed until any increase in average (or maximum) exposure error between iterations or the maximum number of iterations is reached. In each iteration, all regions are corrected. Exposure (local and global) is computed using the PSF layer corresponding to the location of critical point in the 3-D sidewall. Then optimal dose factor for each region is then searched for, which minimizes the cost function given in Equation 4.2.

Thus, the problem of finding a dose distribution to reduce the exposure error belongs to the class of *NP hard* problems (in fact all 3-D correction schemes) and hence a solution is searched by heuristics. The iso-exposure correction problem is approached as a constrained optimization problem wherein an optimal dose factor for each region is searched for, which minimizes the cost function (see Equation 4.2).

The fundamental problem with the 3-D iso-exposure correction (in fact all 3-D correction schemes) is when the thickness of the resist increases, the critical points located at

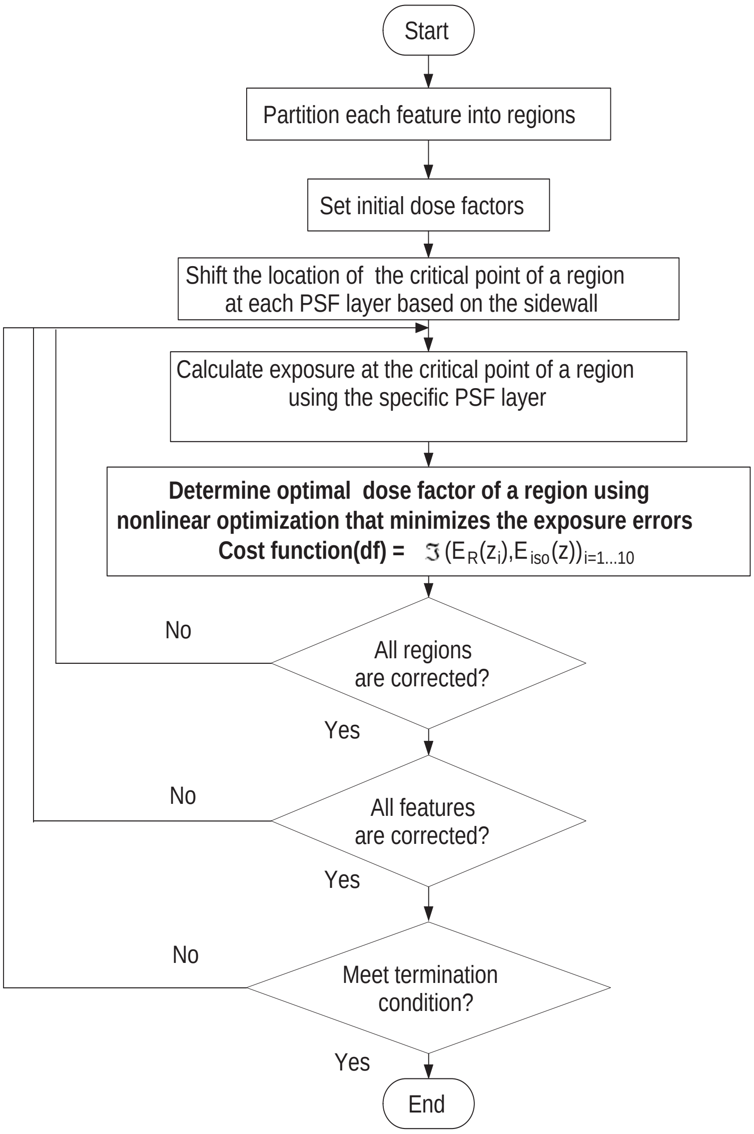

Figure 4.4: Flow chart for 3-D iso-exposure binary correction.

different depths require different dose factors in order to make $E_R(z_i)$ equal to $E_{iso}(z)$. In this study, a simple approach of determining the dose factor for each region, which minimizes the sum of exposure errors in all layers, is taken (refer to Equation 4.2).

As discussed in Section 3.3.3, the actual remaining resist profile does not correspond to any single iso-exposure contour. Therefore, even if a dose distribution which results in an iso-exposure contour matching a target remaining resist profile is found, the actual remaining resist profile is likely to be different from the target profile. In order to make correction results more realistic, the development model described in Section 2.4 is to be employed in correction instead of the exposure model. That is, the estimated remaining resist profile rather than an iso-exposure contour needs to be used as a reference for optimization during correction.

4.3 Resist Profile Correction

4.3.1 Model

3-D resist profile correction is able to correct for CD (binary) specifications by using the resist development simulation described in Section 2.4 and thus the correction results are more realistic.

Considering a long line feature, exposure $e_l(x, z)$ is estimated along the cross-section of the line, from which the resist development rate, $r_l(x, z)$ is computed. Using the resist development model, the remaining resist profile is predicted through simulation. The CD error on each layer is computed and a cost function is then evaluated as a certain combination of the CD errors in the selected layers. Then, the dose of each region is determined such that the cost function is minimized.

4.3.2 Correction

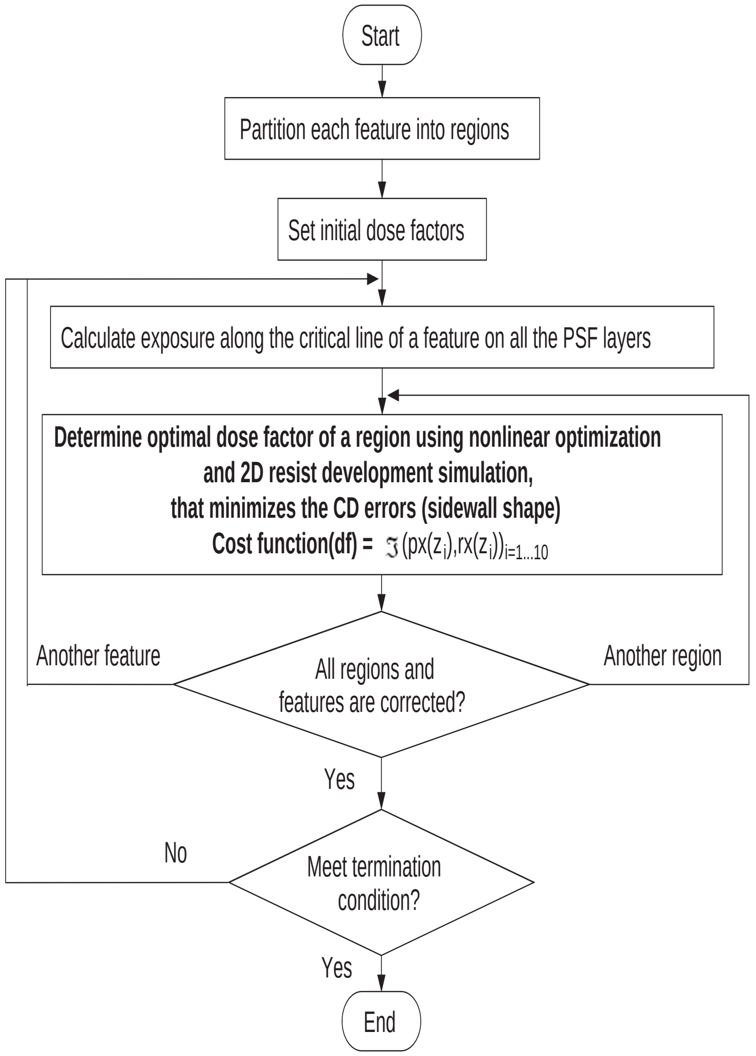

Figure 4.5: Flow chart for 3-D resist profile binary correction

The flowchart in Figure 4.5 shows the steps in 3-D resist profile correction.

In this proof-of-concept implementation correction is performed only along the cross-section of the feature. Thus, the exposure matrix $e_l(x, z)$ is computed only along the critical line (cross-section of the feature) using all the PSF layers as illustrated in Figure 4.6. The

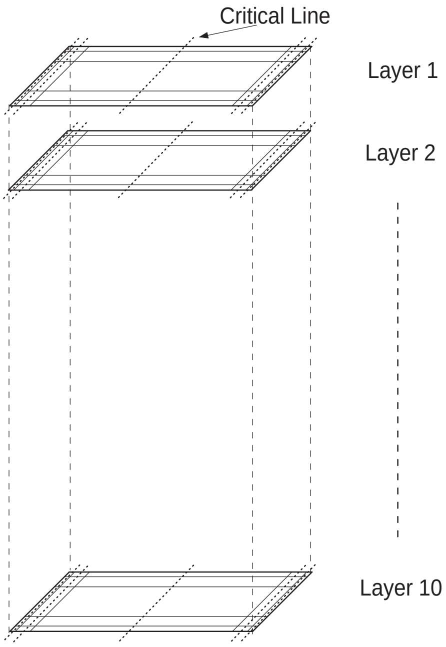

Figure 4.6: 3-D space showing the 10 layers with critical lines along which exposure matrix $e_l(x, z)$ is computed

exposure matrix is then transformed into the rate matrix $r_l(x, z)$ and then the development simulation is used to measure the CD error.

The cost function (see Figure 4.7) is formulated as in Equation 4.3

$$Costfunction(df) = \Im(|(px(z_i) - rx(z_i))|)_{i=0..9} \tag{4.3}$$

where px_i is the actual width (shift) and rx_i is the target width measured from a reference point on the i^{th} layer, and $\Im$ is some function to combine the CD errors in the selected layers. In the current implementation, $\Im$ used is the sum of CD errors in the top, middle and bottom layers only in order to reduce the computational requirement.

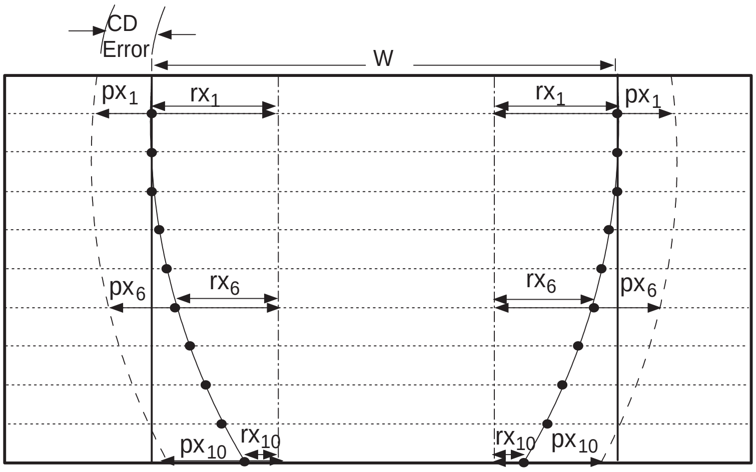

Figure 4.7: Cost function is formulated as a combination of CD errors on all layers, i.e., is given by $\Im(\{rx_i - px_i\})$ where rx_i and px_i are the target and actual widths measured from a reference point on the i^{th} layer.

The dose factor which minimizes the cost function for each region is then determined in a finite number of steps using a search algorithm under the following constraints:

- Dose factor ≥ 0
- Dose factor distribution should meet certain resist development condition or development time

The above correction process is iterated for all regions in a feature using the Equation 4.1. The average CD error for left and right edges of each feature is kept track of and any increase in the average CD error (considering all features in a pattern) between iterations or the maximum number of iterations is then used as the termination condition.

Thus, the problem of finding a dose distribution to reduce the CD error belongs to the class of *NP hard* problems (in fact all 3-D correction schemes) and hence a solution is searched by heuristics. The resist profile correction problem is approached as a constrained optimization problem wherein an optimal dose factor for each region is searched for, which minimizes the cost function (see Equation 4.3).

4.3.3 Multi-layer Multi-region Correction

As mentioned before, the basic correction procedure is a *single-region* correction. Dose for a region is determined based on the error at the corresponding critical point only (errors in no other regions are taken into account). That is, optimization is localized in space. In order to further improve correction accuracy of the basic correction procedure, a *multi-layer multi-region correction* [19] step is added after the regular dose calculation step.

The multi-layer multi-region correction considers multiple neighboring regions within a selection window for different PSF layers as shown in Figure 4.9 when performing correction on a given region. The adjusted dose of the region is chosen to minimize the maximum CD error in its neighbors including the region and, therefore, it tends to balance the correction over the regions as well as the PSF layers. The correction procedure for a given region is described in Figure 4.8.

Several implementation issues are worth mentioning [19]. First, S_{adj} is selected to be smaller than the ring width, because only the regions close to the rectangle boundary are critical to balancing the correction. Second, in deciding whether a region is within the selection window, every region that has any overlap with the window is considered. At last, the multi-layer multi-region correction is not started until the regular correction for the entire circuit is completed (see Figure 4.10) and is iterated with the same termination conditions as for the regular correction. Simulation results shows that this approach can lead a better solution than the regular correction.

```
Set dose factor of current region to be $D_{tmp}$;
Calculate the CD error $Er_{CD}$ using resist development simulation
for all the PSF layers and for all the neighboring regions considered;
Find the maximum CD error $Er_{CDmax}$ from all these $Er_{CD}$;
  if $Er_{CDmax}$>0
        decrease $D_{tmp}$ with a step=$D_{tmp}$/2, until $Er_{CDmax}$<0 or $D_{tmp}$<0;
        if $D_{tmp}$<0 and $Er_{CDmax}$>0 return $D_{tmp}$;
  else if $Er_{CDmax}$<0
        increase $D_{tmp}$ with a step=$D_{tmp}$/2 , until $Er_{CDmax}$>0;
  else if sign of $Er_{CDmax}$ differed between successive iterations
        do:
            step=step/2;
             if $Er_{CDmax}$<0     $D_{tmp}$ = $D_{tmp}$ + step;
             else $D_{tmp}$ = $D_{tmp}$ - step;
             Set dose factor of current region to be $D_{tmp}$ and find $Er_{CDmax}$;
        while step > A (the dose factor resolution);
  return $D_{tmp}$
```

Figure 4.8: Multi-layer Multi-region correction procedure.

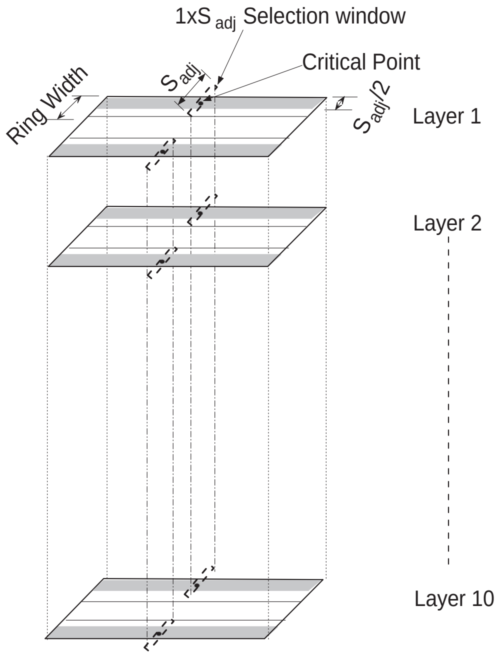

Figure 4.9: Illustration of multi-layer multi-region correction. A rectangle with its partitions are shown for the 10 layers of PSF. Shaded region represents the region where the multi-layer multi-region correction is performed. Selection window is used for selecting the neighbors, while correcting the given region.

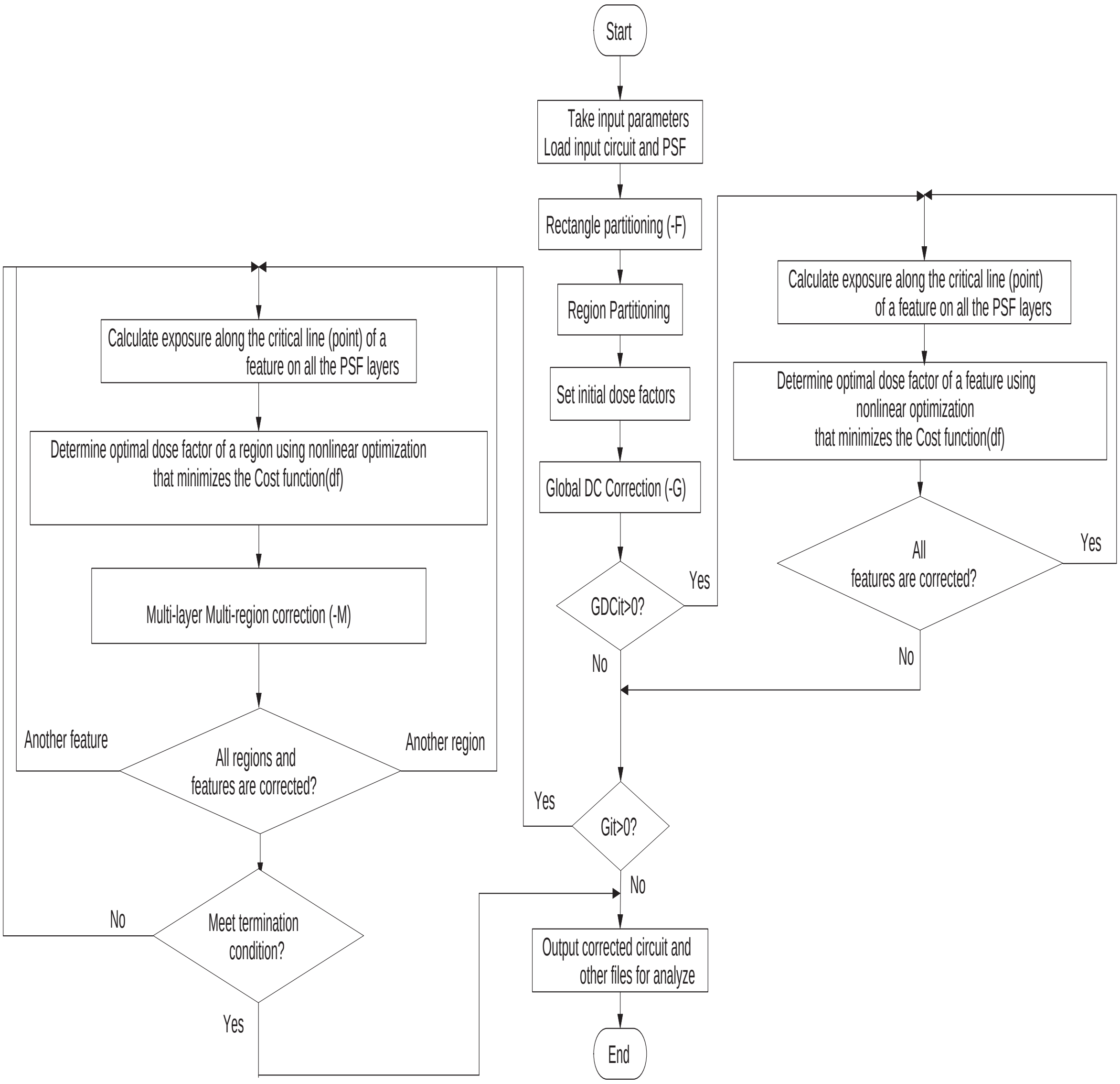

Figure 4.10: Flowchart for regular correction program.

Chapter 5

Comparison of Correction Schemes

The 3-D iso-exposure and resist profile correction schemes have been tested with a variety of line circuit patterns considering the feature size, substrate (PSF) dependency, sidewall shape, and compared to the existing 2-D correction scheme. This chapter contains the computer simulation results and discussion.

All three correction schemes are compared in terms of the remaining resist profiles obtained through the resist development simulation, though the 2-D and 3-D iso-exposure correction schemes use the exposure as the measure to be optimized in correction.

5.1 Error Definition

The *CD error* is used to analyze the accuracy of correction results, which quantifies the difference between the actual and desired remaining resist profiles.

CD Error

The CD error is used to measure how much a feature blurs out or shrinks into its required boundary. For each feature, several *critical points* are set. The distance between the actual boundary and the critical point is measured as the CD error in each layer.

As illustrated in Figure 5.1, there are several critical points located in the 3-D space for each feature. The example in Figure 5.1 is for an overcut resist profile with a line width of W. An average CD error is given by Equation 5.1. Average and maximum CD errors

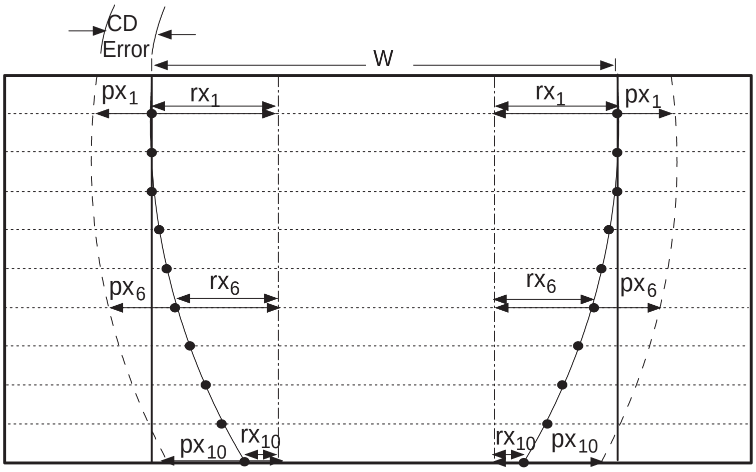

Figure 5.1: Illustration of the critical points for the measurement of CD errors. Desired boundary is given by continuous line, while actual boundary is given by dashed line. CD error is given by $(rx_i - px_i)$ where rx_i and px_i are the target and actual widths measured from a critical point on the i^{th} layer.

are normalized by the feature width W and expressed in percentage to compare the errors with different feature size and are given by Equation 5.2 and Equation 5.3, respectively.

$$Er_{CD} = \frac{\sum_{i=0}^{n_l}(rx_i - px_i)}{n_l} \tag{5.1}$$

where Er_{CD} is the average CD error in nm, and n$_l$ is the number of PSF layers analyzed.

$$\overline{Er}_{CD} = \frac{Er_{CD}}{W} \tag{5.2}$$

$$\overline{Er}_{CDmax} = \frac{Er_{CDmax}}{W} \tag{5.3}$$

where $\overline{Er}_{CD}$ is the normalized average CD error, $\overline{Er}_{CDmax}$ is the normalized maximum CD error, Er_{CDmax} is the maximum CD error in nm, and W is the width of feature in nm.

5.2 Correction Schemes

Three different correction schemes to be compared in terms of their performance are:

- *2-D Binary Correction*: uses the 2-D exposure model ensuring the center region to receive an exposure equal to or greater than the "center exposure" and the boundary pixels to receive 75% of the center exposure.
- *3-D Iso-Exposure Correction*: attempts to match an iso-exposure contour (corresponding to the threshold) with the desired shape of sidewall.
- *3-D Resist Profile Correction*: attempts to achieve the remaining resist profile matching the target sidewall profile under the given development constraint using the resist development model.

5.3 Simulation Results and Discussion

The three different correction schemes are compared on the basis of their resist profiles using the resist development simulation. In the 2-D and 3-D iso-exposure corrections, since there is no reference on development time, overcut and undercut are achieved by setting appropriate resist development conditions in the development simulation as described in the following subsections.

5.3.1 Vertical Sidewall

Vertical sidewall is achieved in the 2-D and 3-D iso-exposure corrections by continuing the resist development simulation until all pixels in a given feature reaches the bottom of resist.

Illustrated in Figure 5.2-(a) and (b) are the vertical iso-exposure contours achieved using the 3-D iso-exposure correction. It is often the case that for certain PSFs characterized by higher proximity effect it is difficult to control an iso-exposure contour to resemble the target sidewall profile as shown in Figure 5.2-(a).

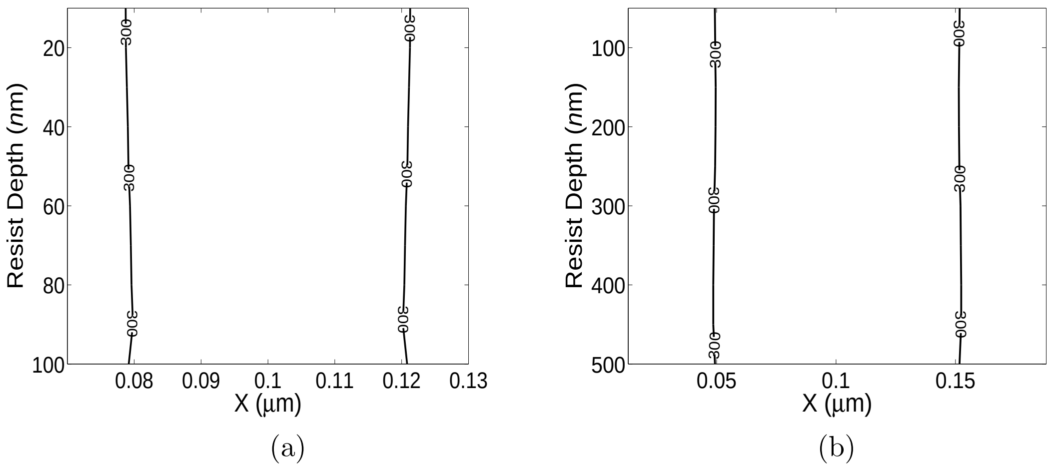

Figure 5.2: Vertical iso-exposure contour with E_i= 300 μ C/cm^2 corrected by 3-D iso-exposure correction: (a) for a line pattern of width 40 nm (100 nm PMMA on Si, 5keV), and (b) for a line pattern of width 100 nm (500 nm PMMA on Si, 20 keV).

In Figures 5.3 and 5.4, some of the simulation results for vertical sidewall are provided, where the remaining resist profiles of a single line are compared. It is clearly seen that those achieved by the 3-D resist profile correction are significantly better than those by the 2-D or 3-D iso-exposure correction. Though the 3-D iso-exposure correction achieves an iso-exposure contour resembling the vertical sidewall in Figure 5.2-(a) and (b), the final resist profiles in Figure 5.3-(b) and Figure 5.4-(b) are still subject to larger CD errors than those for the resist profile correction.

Shown in Tables 5.1 and 5.2 are the CD errors in each layer of the resist. The CD errors for the 3-D resist profile correction are in general much smaller than those for the

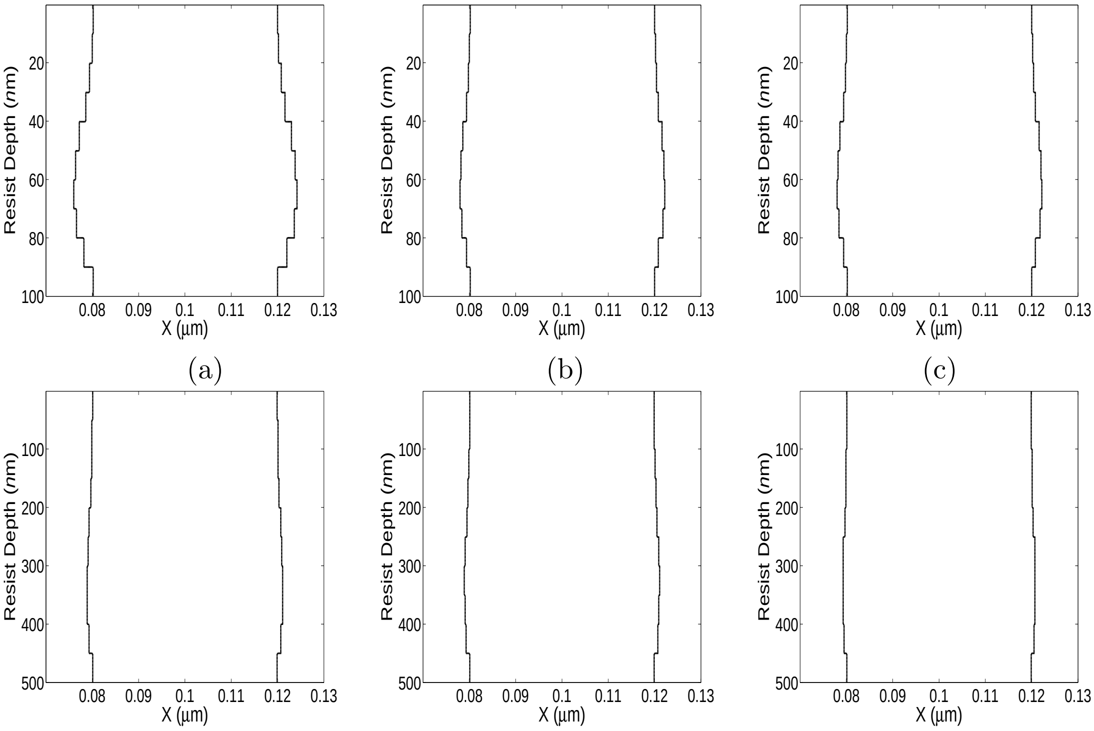

Figure 5.3: Remaining resist profiles (vertical sidewalls) for line width of 40 *n*m for 100 *n*m PMMA on *Si*, 5 keV:(a) 2-D correction, (b) 3-D iso-exposure correction, (c) 3-D resist profile correction, and for 500 *n*m PMMA on *Si*, 50 keV:(d) 2-D correction, (e) 3-D iso-exposure correction, (f) 3-D resist profile correction.

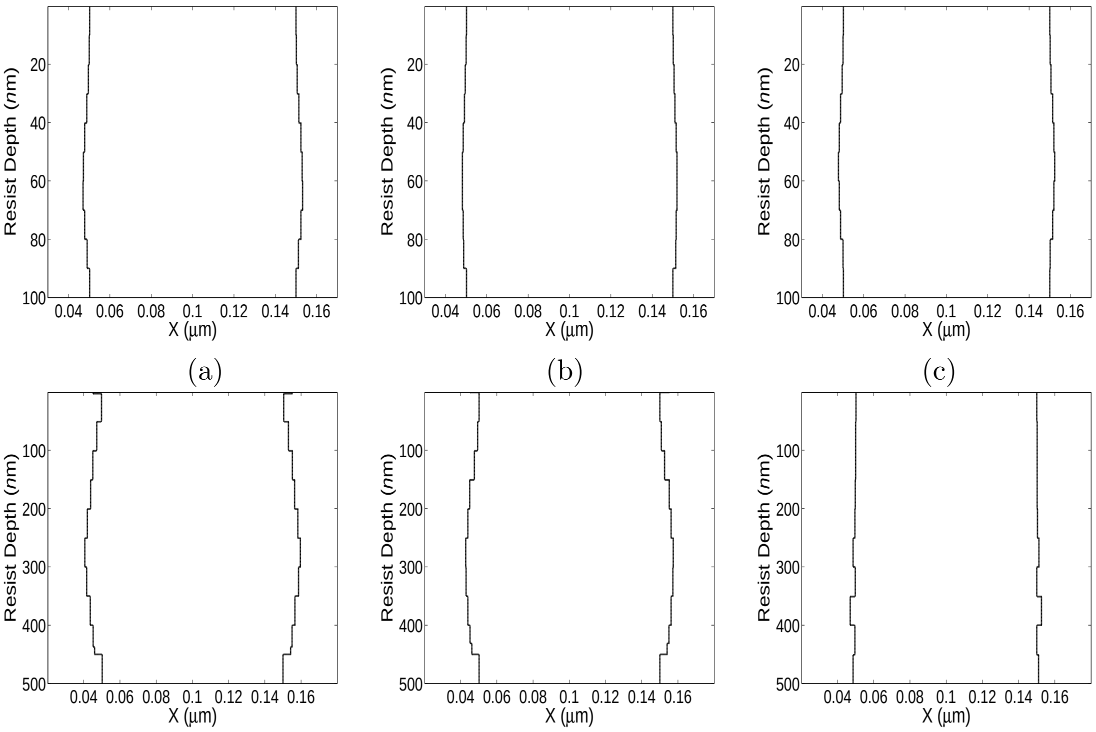

(a) (b) (c)

(d) (e) (f)

Figure 5.4: Remaining resist profiles (vertical sidewalls) for line width of 100 *n*m for 100 *n*m PMMA on *Si*, 5 keV: (a) 2-D correction, (b) 3-D iso-exposure correction, (c) 3-D resist profile correction, and 500 *n*m PMMA on *Si*, 20 keV: (d) 2-D correction, (e) 3-D iso-exposure correction, (f) 3-D resist profile correction.

2-D correction. It is also observed that thicker resist and lower beam energy lead to larger CD errors as expected due to higher intra-proximity effect, so as the case for decreasing feature size. But, again the 3-D resist profile correction is able to reduce the average CD error compared to the other correction schemes, as seen in Figures 5.3-(c) and 5.4-(f), for lower beam energy and thicker resist, respectively.

Layers	**CD Error (nm)**								
	100 nm PMMA, 5 keV			**500 nm PMMA, 50 keV**			**1000 nm PMMA, 50 keV**		
	2-D	**3-D Iso-Exposure**	**3-D Resist Profile**	**2-D**	**3-D Iso-Exposure**	**3-D Resist Profile**	**2-D**	**3-D Iso-Exposure**	**3-D Resist Profile**
1 (Top)	0.083	0.048	0.043	0.123	0.054	0.006	1.653	0.047	0.041
2	0.275	0.161	0.144	0.217	0.096	0.010	5.030	0.201	0.035
3	0.730	0.424	0.383	0.482	0.213	0.022	5.705	1.550	0.481
4	1.679	0.952	0.859	0.929	0.430	0.045	8.209	5.288	2.939
5	2.951	1.675	1.526	1.403	0.690	0.075	10.702	7.711	6.347
6 (Middle)	3.885	2.161	2.041	2.009	1.044	0.115	11.878	10.136	8.929
7	4.298	2.242	2.214	2.285	1.219	0.135	12.340	10.873	10.540
8	3.654	1.917	1.176	2.368	1.172	0.131	10.000	9.207	8.344
9	1.977	0.833	0.833	2.019	0.817	0.098	5.994	5.665	5.601
10 (Bottom)	0.000	0.000	0.000	1.032	0.000	0.000	0.615	0.433	0.390
$\overline{Er}_{CD}$ (%)	4.883	2.603	2.451	3.217	1.434	0.159	18.031	12.778	10.911
$\overline{Er}_{CDmax}$ (%)	10.746	5.604	5.536	5.921	3.048	0.338	30.850	27.183	26.350
Simulation Time (sec)	0.01	0.29	1.48	0.02	0.49	4.06	0.04	0.22	28.5

Table 5.1: Comparison of performance of correction schemes with various PSFs (beam energy and resist thickness) for a feature of line width 40 nm for vertical sidewall.

Layers	**CD Error (nm)**								
	500 nm PMMA, 50 keV			**500 nm PMMA, 20 keV**			**1000 nm PMMA, 50 keV**		
	2-D	**3-D Iso-Exposure**	**3-D Resist Profile**	**2-D**	**3-D Iso-Exposure**	**3-D Resist Profile**	**2-D**	**3-D Iso-Exposure**	**3-D Resist Profile**
1 (Top)	0.181	0.163	0.023	0.642	0.154	0.038	1.612	0.490	0.469
2	0.343	0.309	0.045	3.002	0.795	0.162	5.024	1.867	1.735
3	0.760	0.684	0.083	5.210	2.656	0.259	5.578	5.096	5.051
4	1.395	1.256	0.122	6.369	5.204	0.313	7.390	6.156	5.990
5	2.063	1.865	0.142	8.212	6.130	0.565	10.057	8.144	7.774
6 (Middle)	2.960	2.682	0.266	9.656	7.481	1.538	10.742	9.678	9.074
7	3.352	3.035	0.060	8.628	7.174	0.401	11.045	9.728	9.172
8	3.689	3.316	0.328	6.655	6.126	3.202	8.793	7.290	6.752
9	3.542	3.119	0.400	4.771	4.642	0.595	5.741	4.814	4.747
10 (Bottom)	2.695	2.230	0.553	0.000	0.000	1.600	0.647	0.000	0.000
$\overline{Er}_{CD}$ (%)	2.098	1.866	0.202	5.314	4.036	0.867	6.662	5.326	5.076
$\overline{Er}_{CDmax}$ (%)	3.689	3.316	0.553	9.656	7.481	3.202	11.045	9.728	9.172
Simulation Time (sec)	0.02	0.49	5.36	0.02	0.22	26.00	0.06	0.24	31.5

Table 5.2: Comparison of performance of correction schemes with various PSFs (beam energy and resist thickness) for a feature of line width 100 nm for vertical sidewall.

Illustrated in Figure 5.5 are the correction results of feature of width 10 *nm*. The pixel is reduced from 5 *nm* to 1 *nm* to increase the accuracy of development simulation. Again, it is seen that the 3-D resist profile correction is able to reduce both the maximum and average CD errors compared to the other schemes though the achieved sidewalls are substantially different from being vertically straight.

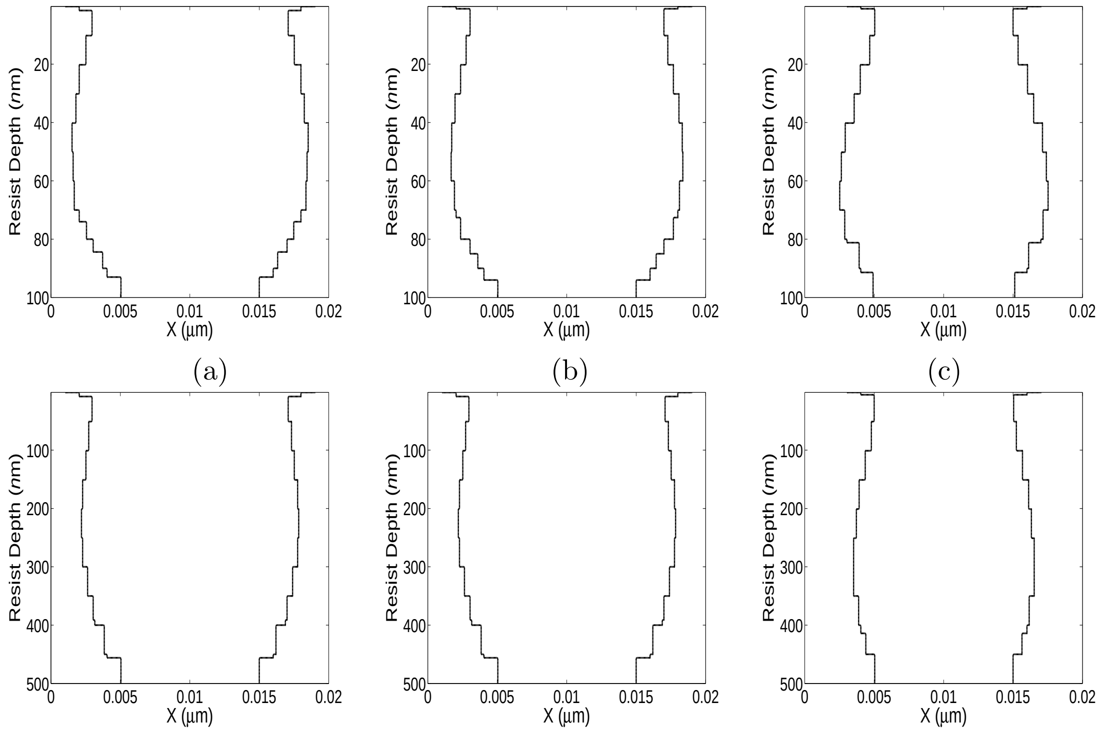

(a) (b) (c)

(d) (e) (f)

Figure 5.5: Remaining resist profiles (vertical sidewalls) for line width of 10 nm for 100 nm PMMA on Si, 5 keV:(a) 2-D correction, (b) 3-D iso-exposure correction, (c) 3-D resist profile correction, and for 500 nm PMMA on Si, 20 keV:(d) 2-D correction, (e) 3-D iso-exposure correction, (f) 3-D resist profile correction.

5.3.2 Overcut Sidewall

Overcut is achieved in the 2-D binary PYRAMID by decreasing the base dose. Since, there is no quantitative control on sidewall shape in 2-D correction, the resist development proceeds until an overcut profile is achieved.

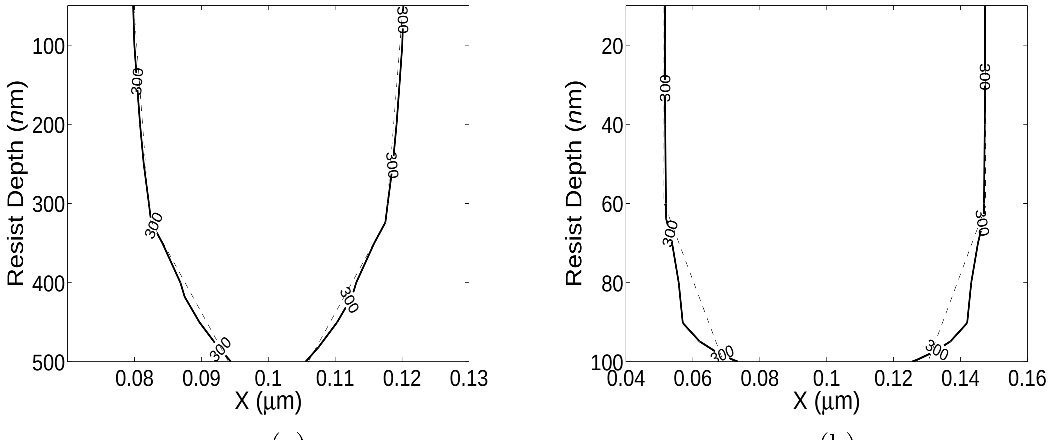

(a) (b)

Figure 5.6: Overcut iso-exposure contour with E_i= 300 μ C/cm^2 corrected by 3-D iso-exposure correction:(a) for a line pattern of width 40 nm (500 nm PMMA on Si, 50 keV, with rx_1=0 nm, rx_5=5 nm, and rx_{10}=15 nm), and (b) for a line pattern of width 100 nm (100 nm PMMA on Si, 50 keV, with rx_1=0 nm, rx_5=0 nm, and rx_{10}=20 nm).

In Figures 5.7 and 5.8 the dashed lines indicate the desired sidewall to be achieved. In the 2-D correction results, it can be seen that the CD specification is well matched only at the top layer, but larger CD errors are observed in almost all of the other layers including the bottom layer. No significant improvement has been achieved by the 3-D iso-exposure correction in spite of iso-exposure contours meeting the target resist profiles as seen in Figure 5.6-(a) and (b) corresponding to the final development profiles in Figure 5.7-(e) and Figure 5.8-(b), respectively. However, the remaining resist profiles obtained by the 3-D resist profile correction are much closer to the target profiles.

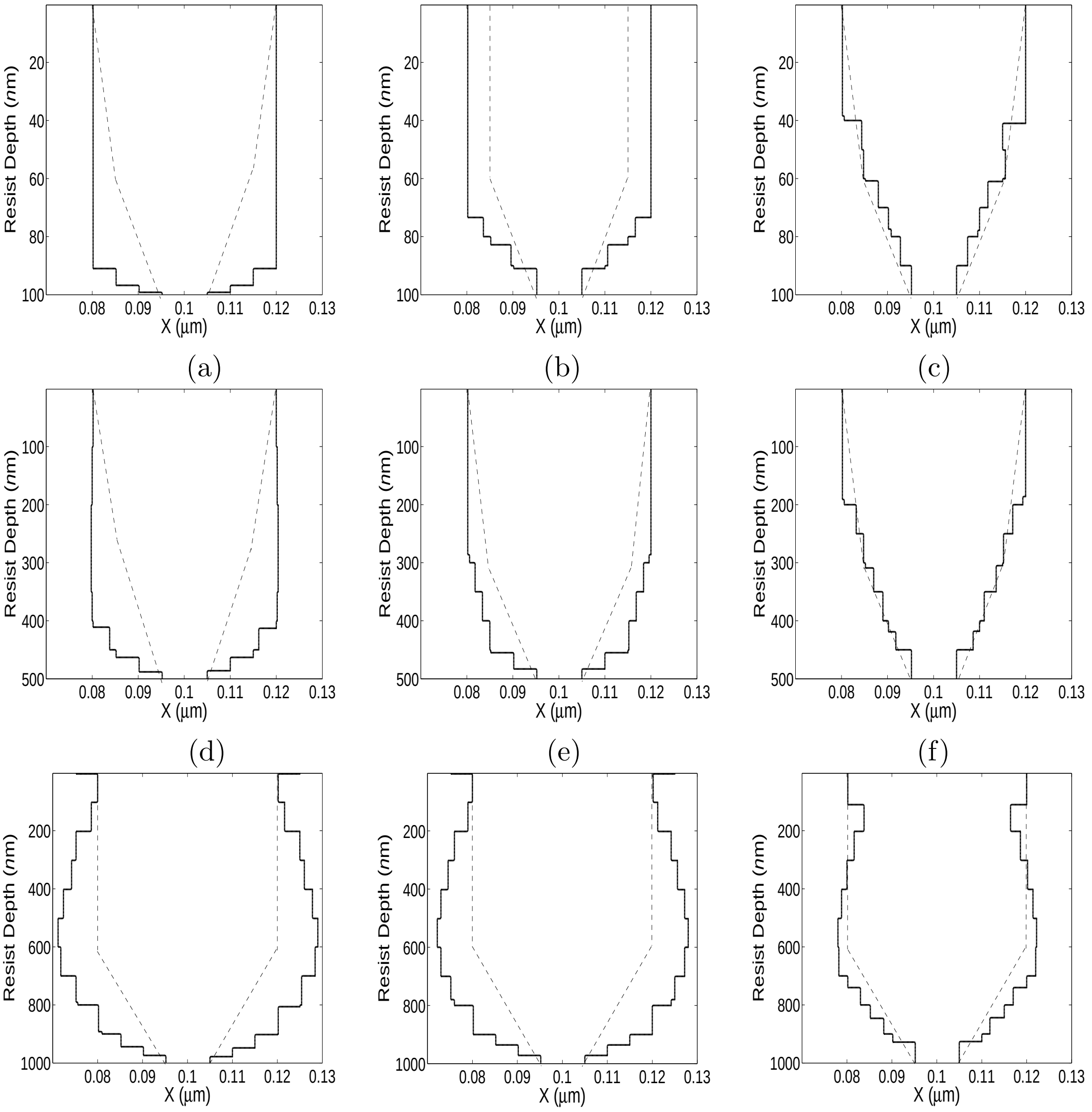

(a) (b) (c)

(d) (e) (f)

(g) (h) (i)

Figure 5.7: Remaining resist profiles (overcut) for line width of 40 *n*m: (100 *n*m PMMA on *Si*, 20 keV, with rx_1=0 *n*m, rx_5=5 *n*m, and rx_{10}=15 *n*m) (a) 2-D correction, (b) 3-D iso-exposure correction, (c) 3-D resist profile correction; (500 *n*m PMMA on *Si*, 50 keV, with rx_1=0 *n*m, rx_5=5 *n*m, and rx_{10}=15 *n*m) (d) 2-D correction, (e) 3-D iso-exposure correction, (f) 3-D resist profile correction; (1000 *n*m PMMA on *Si*, 50 keV, with rx_1=0 *n*m, rx_5=0 *n*m, and rx_{10}=15 *n*m) (g) 2-D correction, (h) 3-D iso-exposure correction, (i) 3-D resist profile correction.

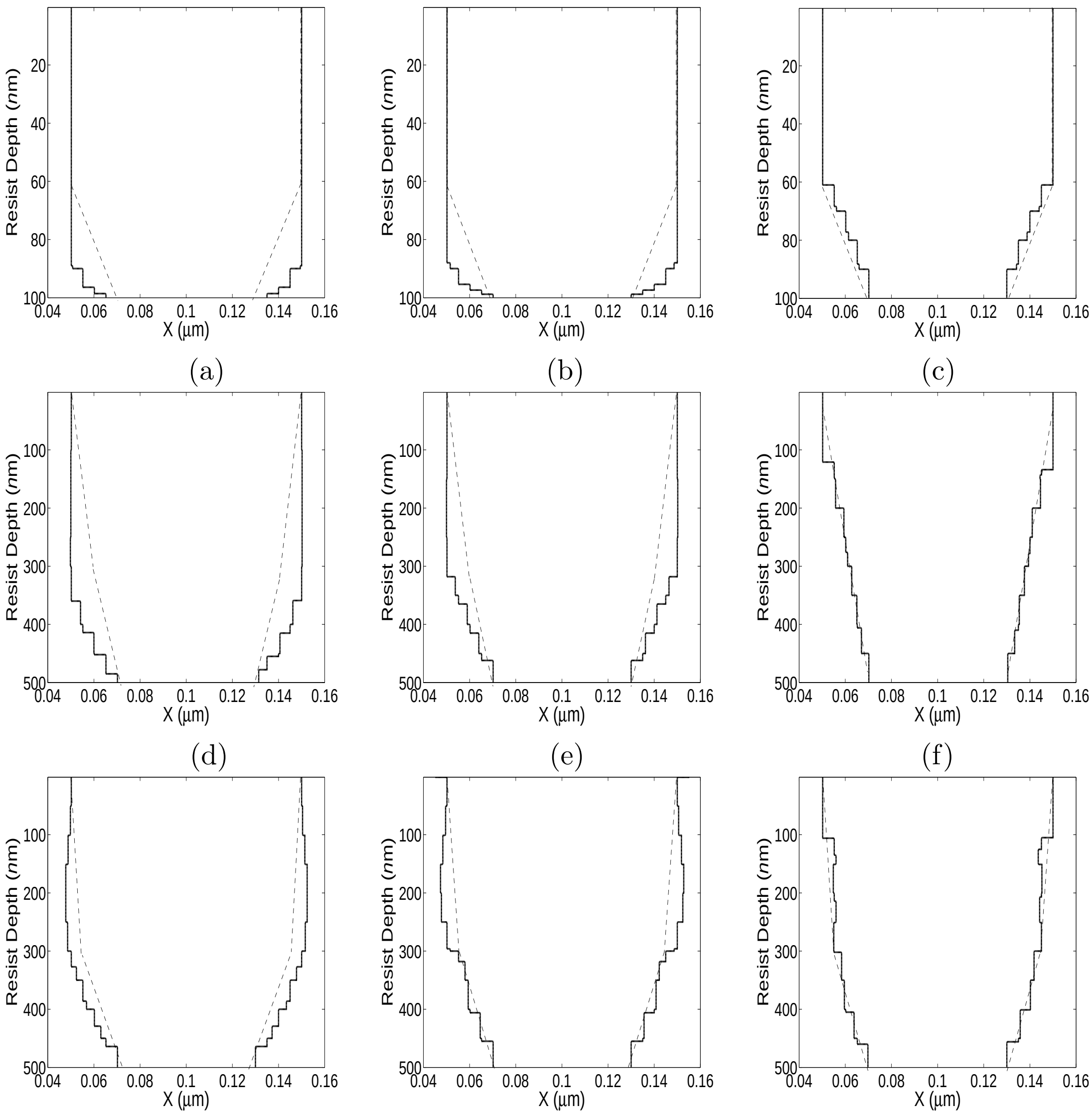

(a) (b) (c)

(d) (e) (f)

(g) (h) (i)

Figure 5.8: Remaining resist profiles (overcut) for line width of 100 *n*m: (100 *n*m PMMA on *Si*, 50 keV, with rx_1=0 *n*m, rx_5=0 *n*m, and rx_{10}=20 *n*m) (a) 2-D correction, (b) 3-D iso-exposure correction, (c) 3-D resist profile correction; (500 *n*m PMMA on *Si*, 50 keV, with rx_1=0 *n*m, rx_5=10 *n*m, and rx_{10}=20 *n*m) (d) 2-D correction, (e) 3-D iso-exposure correction, (f) 3-D resist profile correction; and (500 *n*m PMMA on *Si*, 20 keV, with rx_1=0 *n*m, rx_5=5 *n*m, and rx_{10}=20 *n*m) (g) 2-D correction, (h) 3-D iso-exposure correction, (i) 3-D resist profile correction.

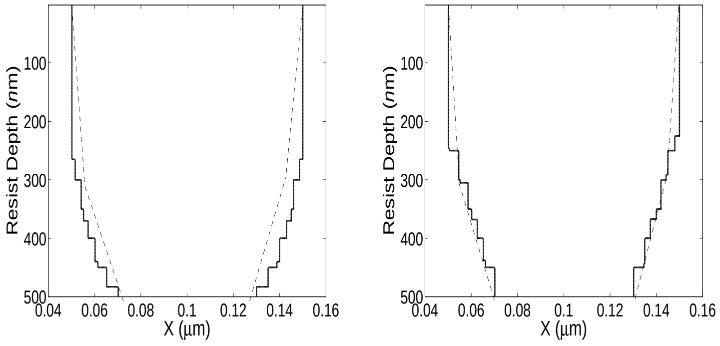

(a) (b)

Figure 5.9: Remaining resist profiles (overcut) for line width of 100 nm (500 nm PMMA on Si, 50 keV) (a) 3-D iso-exposure correction, and (b) 3-D resist profile correction with rx_1=0 nm, rx_5=5 nm, and rx_{10}=20 nm.

Shown in Figure 5.9 is the improved CD controllability in a specific layer. Here, it is tried to adjust the CD requirement of middle layer by fixing the top and bottom CD requirements to be the same as those in Figure 5.8-(f). It is seen that the 3D iso-exposure correction results in (refer to Figure 5.9-(a)) CD errors in the middle and bottom layers which are 4 nm and 3.3 nm, respectively, while the 3-D resist profile correction (refer Figure 5.9-(b)) is able to meet the requirements very closely. The 2-D correction would give the same result as that of Figure 5.8-(d), thus highlighting the limitations of the 2-D correction scheme.

Tables 5.3 and 5.4 summarize the performance improvement by the 3-D correction schemes over the 2-D correction for overcut sidewall.

Layers	**CD Error (nm)**								
	100 nm PMMA, 20 keV			**500 nm PMMA, 50 keV**			**1000 nm PMMA, 50 keV**		
	2-D	**3-D Iso-Exposure**	**3-D Resist Profile**	**2-D**	**3-D Iso-Exposure**	**3-D Resist Profile**	**2-D**	**3-D Iso-Exposure**	**3-D Resist Profile**
Top	0.00	0.00	0.00	0.00	0.00	0.00	0.00	0.40	0.00
Middle	5.02	5.00	0.34	5.50	4.90	0.40	9.00	8.00	2.30
Bottom	8.50	0.30	0.00	5.10	3.70	0.00	6.00	5.40	0.90
$\overline{Er}_{CD}$ (%)	11.26	4.42	0.28	8.83	7.16	0.33	12.50	11.50	2.66
$\overline{Er}_{CDmax}$ (%)	21.25	12.50	0.85	13.75	12.25	1.00	22.50	20.00	5.75
Simulation Time (sec)	0.01	0.29	0.30	0.02	0.49	4.36	0.02	0.49	25.36

Table 5.3: Comparison of performance of correction schemes with various PSFs (beam energy and resist thickness) for a feature of line width 40 nm for an overcut sidewall.

Layers	**CD Error (nm)**								
	100 nm PMMA, 50 keV			**500 nm PMMA, 50 keV**			**500 nm PMMA, 20 keV**		
	2-D	**3-D Iso-Exposure**	**3-D Resist Profile**	**2-D**	**3-D Iso-Exposure**	**3-D Resist Profile**	**2-D**	**3-D Iso-Exposure**	**3-D Resist Profile**
Top	0.00	0.00	0.00	0.00	0.00	0.00	0.00	0.00	0.00
Middle	0.00	0.00	0.00	10.00	10.00	0.00	6.60	4.90	0.01
Bottom	12.50	10.80	0.00	3.78	1.20	0.01	1.40	0.40	0.01
$\overline{Er}_{CD}$ (%)	4.16	3.60	0.00	4.59	3.73	0.00	2.67	1.77	0.01
$\overline{Er}_{CDmax}$ (%)	12.50	10.80	0.00	10.00	10.00	0.01	6.60	4.90	0.01
Simulation Time (sec)	0.03	0.29	0.93	0.03	0.49	5.25	0.03	0.59	30.52

Table 5.4: Comparison of performance of correction schemes with various PSFs (beam energy and resist thickness) for a feature of line width 100 nm for an overcut sidewall.

Illustrated in Figure 5.10 are the correction results of feature width of 10 *nm*. Again, it is seen that the 3-D resist profile correction is able to reduce both the maximum and average CD errors compared to the other schemes.

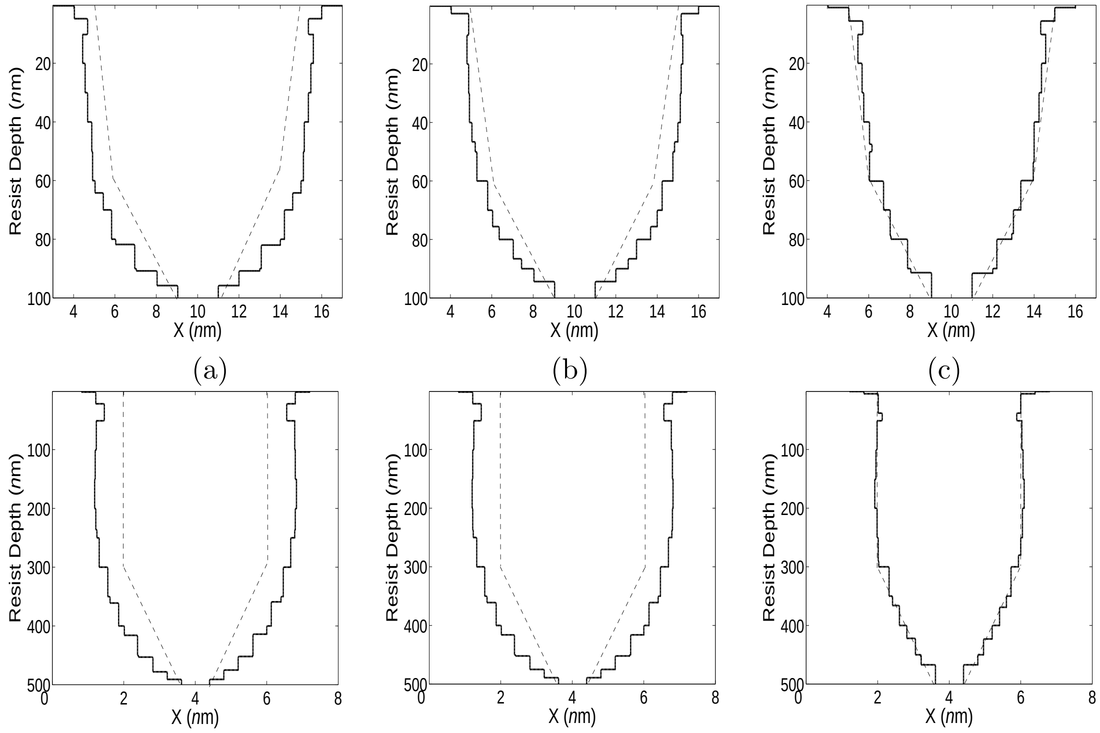

(a) (b) (c)

(d) (e) (f)

Figure 5.10: Remaining resist profiles (overcut) for line width of 10 nm: (100 nm PMMA on Si, 50 keV, with rx_1=0 nm, rx_5=1 nm, and rx_{10}=4 nm) (a) 2-D correction, (b) 3-D iso-exposure correction, (c) 3-D resist profile correction, and (500 nm PMMA on Si, 50 keV, with rx_1=0 nm, rx_5=0 nm, and rx_{10}=4 nm) (d) 2-D correction, (e) 3-D iso-exposure correction, (f) 3-D resist profile correction.

5.3.3 Undercut Sidewall

Undercut is achieved in the 2-D binary PYRAMID by increasing the base dose. Since, there is no quantitative control on sidewall shape in 2-D correction, the resist development proceeds until an undercut profile is met.

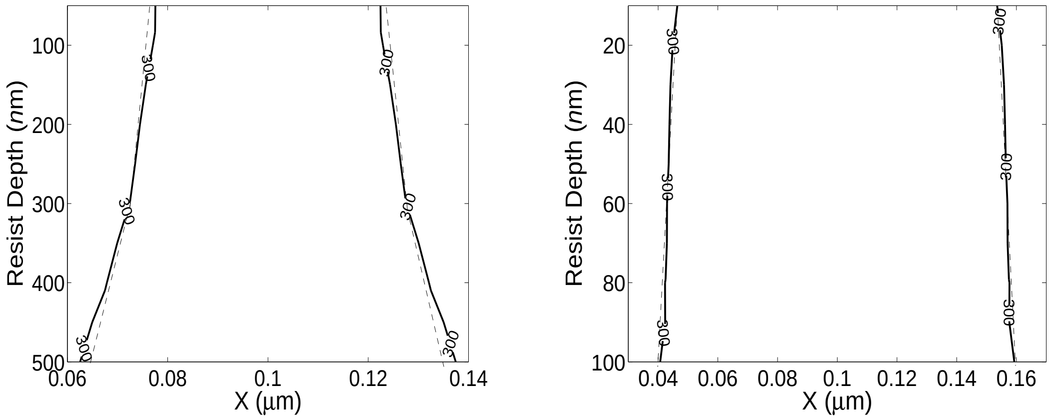

Figure 5.11: Undercut iso-exposure contour with E_i= 300 μ C/cm^2 corrected by 3-D iso-exposure correction:(a) for a line pattern of width 40 *n*m (500 *n*m PMMA on *Si*, 50 keV, with rx_1=5 *n*m, rx_5=10 *n*m, and rx_{10}=20 *n*m), and (b) for a line pattern of width 100 *n*m (100 *n*m PMMA on *Si*, 5 keV, with rx_1=5 *n*m, rx_5=7.5 *n*m, and rx_{10}=10 *n*m).

In Figures 5.12 and 5.13, simulation results for undercuts are presented with the targeted undercut profiles indicated by the dashed lines. Figures 5.11-(a) and (b) show the iso-exposures corresponding to Figure 5.12-(e) and Figure 5.13-(b), respectively. One can notice a substantial difference between the target and actual profiles in the top and middle layers in the cases of the 2-D and 3-D iso-exposure correction results while there is no such difference in the 3-D resist profile correction results.

In Figure 5.14, the improved CD controllability in the bottom layer by the 3-D resist profile correction is shown, by fixing the top and middle CD requirements to be the same as those in Figure 5.12-(f).

Tables 5.5 and 5.6 summarize the performance improvement by the 3-D correction schemes over the 2-D correction for undercut sidewall.

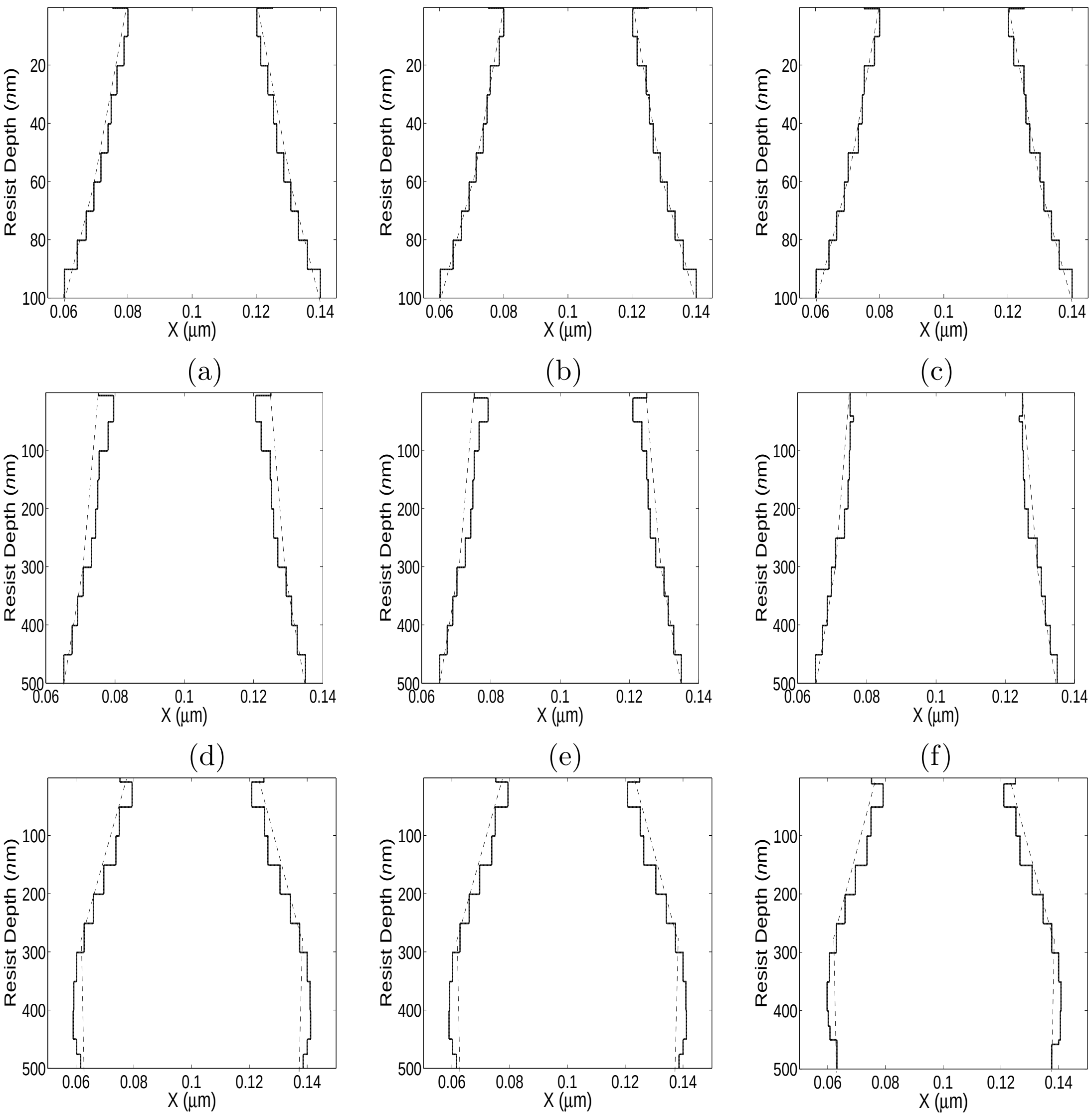

(a) (b) (c)

(d) (e) (f)

(g) (h) (i)

Figure 5.12: Remaining resist profiles (undercut) for line width of 40 nm: (100 nm PMMA on Si, 5 keV, with rx_1=0 nm, rx_5=10 nm, and rx_{10}=20 nm) (a) 2-D correction, (b) 3-D iso-exposure correction, (c) 3-D resist profile correction;(500 nm PMMA on Si, 50 keV, with rx_1=5 nm, rx_5=10 nm, and rx_{10}=15 nm) (d) 2-D correction, (e) 3-D iso-exposure correction, (f) 3-D resist profile correction; (500 nm PMMA on Si, 20 keV, with rx_1=5 nm, rx_5=15 nm, and rx_{10}=15 nm) (g) 2-D correction, (h) 3-D iso-exposure correction (i) 3-D resist profile correction.

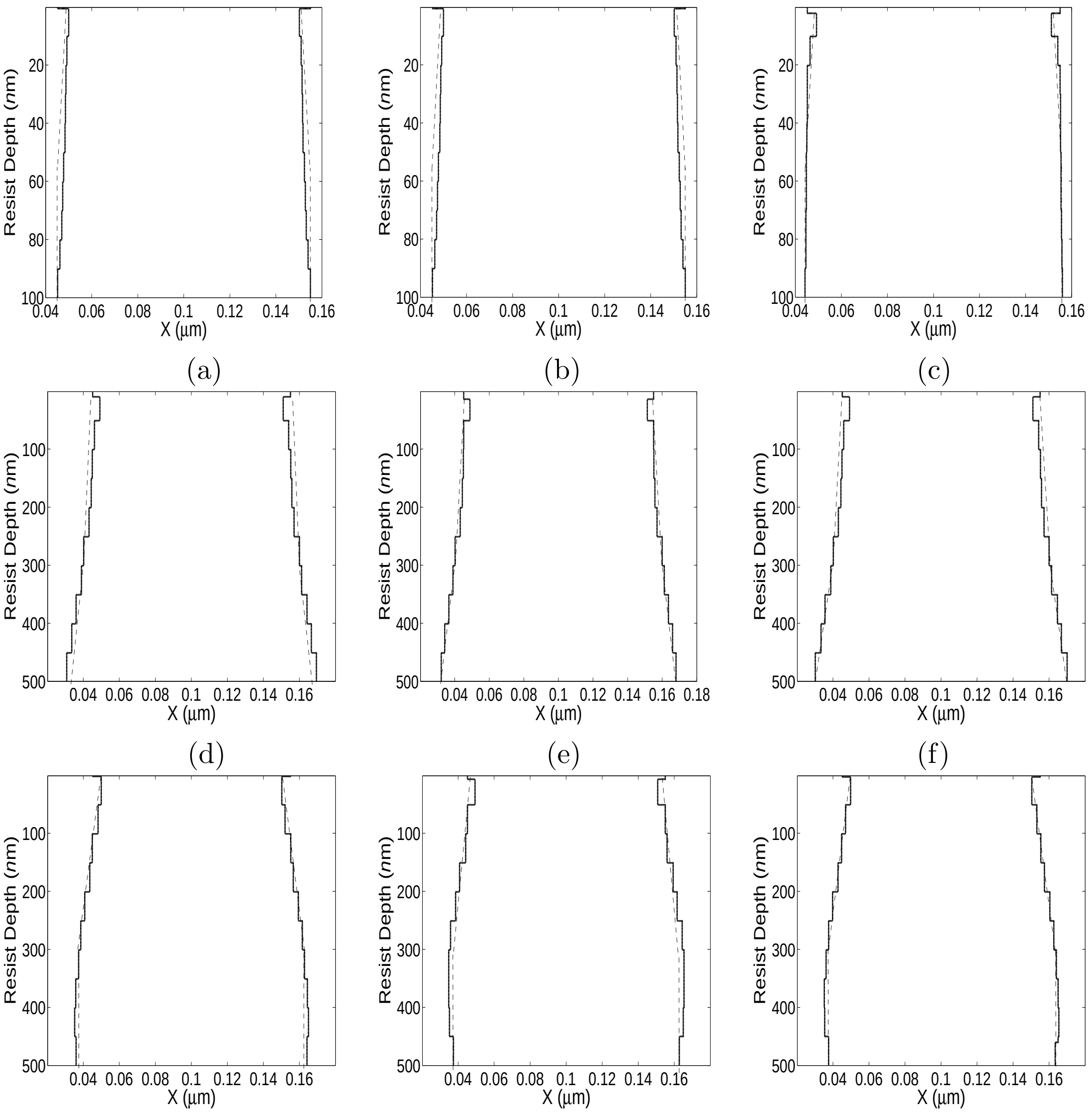

(a) (b) (c)

(d) (e) (f)

(g) (h) (i)

Figure 5.13: Remaining resist profiles (undercut) for line width of 100 nm: (100 nm PMMA on Si, 5 keV, with rx_1=5 nm, rx_5=7.5 nm, and rx_{10}=10 nm) (a) 2-D correction, (b) 3-D iso-exposure correction, (c) 3-D resist profile correction; (500 nm PMMA on Si, 50 keV, with rx_1=5 nm, rx_5=10 nm, and rx_{10}=20 nm) (d) 2-D correction, (e) 3-D iso-exposure correction, (f) 3-D resist profile correction; (500 nm PMMA on Si, 20 keV, with rx_1=0 nm, rx_5=12.5 nm, and rx_{10}=12.5 nm) (g) 2-D correction, (h) 3-D iso-exposure correction, (i) 3-D resist profile correction.

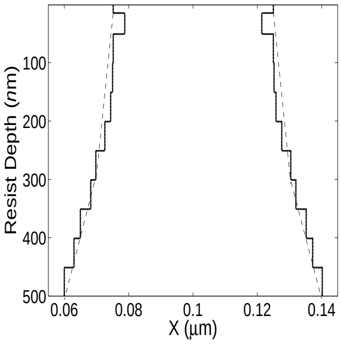

Figure 5.14: Remaining resist profiles (undercut) for line width of 40 nm (500 nm PMMA on Si, 50 keV) using 3-D resist profile correction with rx_1=5 nm, rx_5=10 nm, and rx_{10}=20 nm.

Layers	**CD Error (nm)**								
	100 nm PMMA, 50 keV			**500 nm PMMA, 20 keV**			**1000 nm PMMA, 50 keV**		
	2-D	**3-D Iso-Exposure**	**3-D Resist Profile**	**2-D**	**3-D Iso-Exposure**	**3-D Resist Profile**	**2-D**	**3-D Iso-Exposure**	**3-D Resist Profile**
Top	1.50	0.00	0.20	3.90	3.00	0.13	0.00	0.00	0.00
Middle	1.70	1.90	0.20	3.00	2.30	0.80	1.90	1.80	1.38
Bottom	0.00	0.00	0.00	0.00	0.00	0.00	5.00	4.75	0.00
$\overline{Er}_{CD}$ (%)	2.67	1.50	0.33	5.75	4.41	0.77	5.75	5.46	1.14
$\overline{Er}_{CDmax}$ (%)	4.25	4.50	0.50	9.75	7.50	2.00	12.50	11.88	3.44
Simulation Time (sec)	0.01	0.50	12.29	0.02	0.62	22.46	0.02	0.62	20.00

Table 5.5: Comparison of performance of correction schemes with various PSFs (beam energy and resist thickness) for a feature of line width 40 nm for an undercut sidewall.

Layers	**CD Error (nm)**								
	100 nm PMMA, 50 keV			**500 nm PMMA, 20 keV**			**1000 nm PMMA, 50 keV**		
	2-D	**3-D Iso-Exposure**	**3-D Resist Profile**	**2-D**	**3-D Iso-Exposure**	**3-D Resist Profile**	**2-D**	**3-D Iso-Exposure**	**3-D Resist Profile**
Top	2.00	2.00	0.55	0.75	0.00	0.25	1.50	1.80	0.20
Middle	2.70	2.60	0.30	0.00	0.00	0.50	1.70	0.00	0.30
Bottom	0.10	0.00	0.90	1.80	1.00	0.00	0.00	0.00	0.00
$\overline{Er}_{CD}$ **(%)**	1.60	1.53	0.58	0.85	0.33	0.25	1.07	0.60	0.16
$\overline{Er}_{CDmax}$ **(%)**	2.70	2.60	0.90	1.80	1.00	0.50	1.70	1.80	0.30
Simulation Time (sec)	0.01	0.50	10.18	0.02	0.62	8.62	0.02	0.70	24.20

Table 5.6: Comparison of performance of correction schemes with various PSFs (beam energy and resist thickness) for a feature of line width 100 nm for an undercut sidewall.

In general, it is observed that the 3-D resist profile correction is better than the other two correction schemes. The 3-D iso-exposure correction still results in higher average CD errors than the 3-D resist profile correction. Thus, the iso-exposure correction results support the fact that as the resist thickness increases or line patterns are subject to more intra/inter-proximity effect, the development process must be taken into account for accurate proximity effect correction.

The 3-D resist profile correction is consistently able to perform better than the other schemes with an average CD error less than 2.00 % in most of the cases, but with the increased computational requirement. The computation time is longer for the hard-to-correct PSFs since the feature is partitioned into more regions for better controllability. Also, shown in Table 5.7 are the results showing the performance improvement in terms of CD error by the multi-layer multi-region correction over the single region correction.

	Basic Correction	**Basic +M Correction**	**Basic Correction**	**Basic +M Correction**
	L=40 nm , 1000 nm PMMA, 50 keV, with rx_1= 0 nm, rx_5= 7.5 nm, and rx_{10}= 20 nm		**L=40 nm, 500 nm PMMA, 50 keV, with rx_1=2.5 nm, rx_5=7.5 nm, and rx_{10}=15 nm**	
Layers	**CD Error (nm)**	**CD Error (nm)**	**CD Error (nm)**	**CD Error (nm)**
Top	**0.00**	**0.25**	**0.45**	**0.45**
Middle	**0.60**	**0.25**	**0.61**	**0.25**
Bottom	**1.00**	**0.30**	**0.55**	**0.25**
$\overline{Er}_{CD}$ (%)	**1.34**	**0.67**	**1.34**	**0.79**
$\overline{Er}_{CDmax}$ (%)	**2.50**	**0.75**	**1.53**	**1.13**

Table 5.7: Comparison of performance of the basic resist profile (single region) correction and the basic resist profile with multi-layer multi-region correction for overcut and undercut, respectively

5.3.4 Three-line pattern

In Figure 5.15, the remaining resist profiles of a 3-line pattern corrected for 1000 nm PMMA on Si (50 keV) are shown, where vertical sidewalls are to be achieved. The line width is 50 nm and the space between lines is 40 nm. The 2-D correction result shows a significant inter-proximity effect in the middle layers where the lines are almost merged. However, the result by the 3-D resist profile correction exhibits substantially less inter-proximity effect, and the sidewalls are more vertical than those obtained by the 2-D and 3-D iso-exposure corrections. Controlling sidewall shape can also help improving resolution or feature density especially in the case of vertical sidewall. Note that features can be placed closer to each other when sidewalls are more vertical.

Similarly, results are shown for the overcut and undercut resist profiles in Figure 5.16 and Figure 5.17, respectively. Again, it is seen that the 3-D correction schemes are better than the 2-D correction in controlling the sidewall shape.

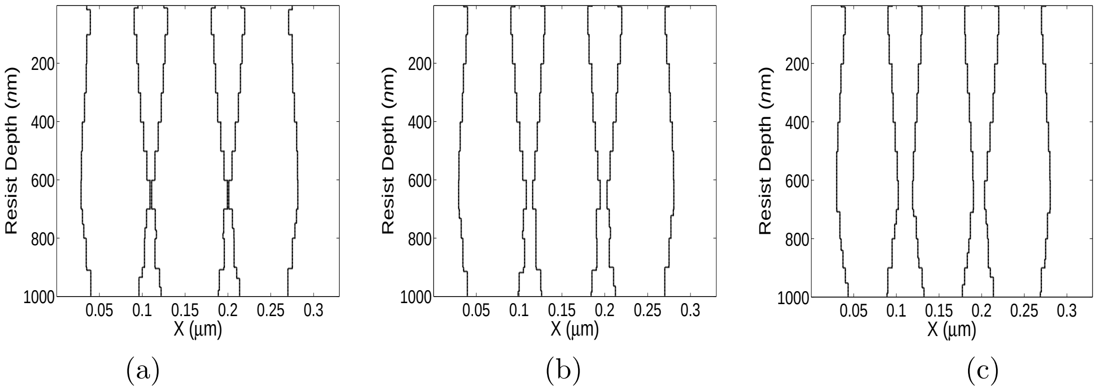

(a) (b) (c)

Figure 5.15: Remaining resist profiles (vertical sidewalls) for a 3-line pattern (L/S=50/40 nm, 1000 nm PMMA on Si, 50 keV) (a) 2-D correction, (b) 3-D iso-exposure correction and (c) 3-D resist profile correction.

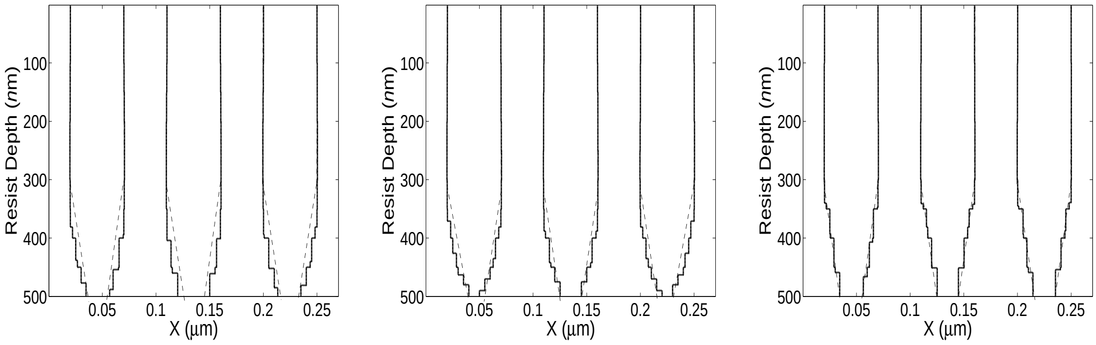

(a) (b) (c)

Figure 5.16: Remaining resist profiles (overcut) for a 3-line pattern (L/S=50/40 nm, 500 nm PMMA on Si, 50 keV, with rx_1=0 nm, rx_5=0 nm, and rx_{10}=15 nm) (a) 2-D correction, (b) 3-D iso-exposure correction and (c) 3-D resist profile correction.

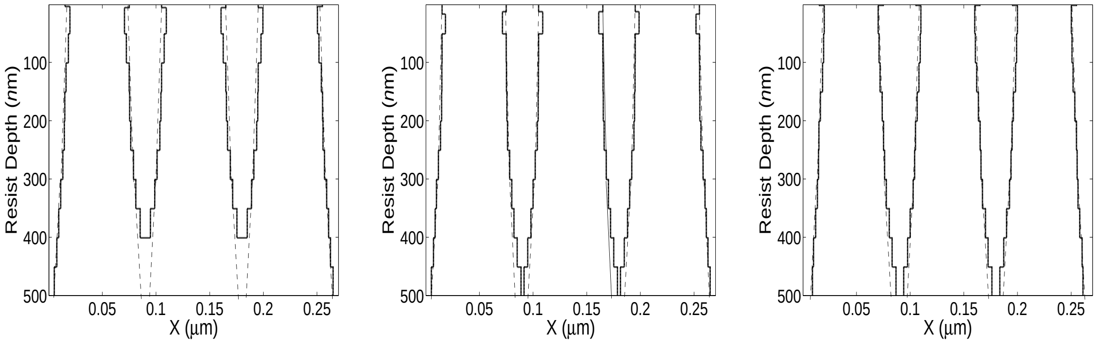

(a) (b) (c)

Figure 5.17: Remaining resist profiles (undercut) for a 3-line pattern (L/S=50/40 nm, 500 nm PMMA on Si, 50 keV, with rx_1=2.5 nm, rx_5=7.5 nm, and rx_{10}=15 nm) (a) 2-D correction, (b) 3-D iso-exposure correction and (c) 3-D resist profile correction.

Chapter 6

Concluding Remarks and Future Study

In this thesis, 3-D proximity effect is analyzed considering the various parameters such as beam energy, resist thickness, feature size, developing threshold., etc., affecting the 3-D spatial distribution of exposure for simple line patterns. The approximation of using the 2-D exposure model leads to significant CD errors in sidewall control and hence an explicit control of 3-D exposure distribution in the resist is required to achieve high dimensional accuracy of the developed patterns.

Two proof-of-concept implementations of 3-D proximity effect correction (iso-exposure contour and resist profile) are described and a detailed analysis of their performance in comparison with the 2-D correction scheme has been carried out via computer simulation for simple line patterns. The iso-exposure contour correction, in spite of achieving the iso-exposure contour resembling the sidewall shape, mostly results in larger CD errors than those by the resist profile correction. In general, the proposed 3-D proximity effect correction has better performance than the 2-D correction in minimizing the CD error and controlling the sidewall shape. Simulation results indicate that the 3-D proximity effect correction schemes described in this thesis, particulary the resist profile correction, has a good potential to control sidewall shape for binary circuit patterns.

The optimization technique (golden section search) used in the 3-D correction schemes is for convex problems though finding the optimum dose distribution is not a convex problem. It was employed mainly to minimize the complexity of the optimization. Hence, there can be a substantial improvement in performance if an appropriate method is adopted. One of the drawbacks of the 3-D resist profile correction is its intensive computation required for the resist development simulation. In order to make it practical an efficient simulation method will need to be developed.

The concept of 3-D resist profile correction may be applicable for correcting *grayscale* circuit patterns (structures with multiple levels).

Appendix A

Implementation

In this Appendix, the unit of exposure and constants associated with the resist development modeling are described.

A.1 Unit of exposure

In other versions of the PYRAMID software, the exposure was scaled to express it in the unit of dose ($\mu C/cm^2$). In this study, the exposure is expressed in eV/μm^3 to employ the resist development simulation. Given a pixel size and a base dose, a PSF (eV/cm^3/e$^-$) is scaled to derive PSF$_{eV}$ as shown in Equation A.1. PSF$_{eV}$ is then employed in the discrete convolution for exposure estimation.

$$PSF_{eV}(r,z) = (PSF(r,z) \cdot d \cdot p \cdot p)/(1.6 \times 10^{-19}) \tag{A.1}$$

where $PSF_{eV}(r,z)$ is in eV/μm^3; $PSF(r,z)$ is in eV/cm^3/e$^-$; d is the basedose in $\mu C/cm^2$; p is pixel size in cm; 1.6×10^{-19} is the electric charge in an electron in $Coulomb$.

A.2 Resist Development Modeling Constants

The following Table A.1 and Table A.2 show the constants for modeling the resist development process based on time-independent threshold solubility and time-dependent cell removal model, respectively.

Reference	Solvent	E$_T$$(eV/cm^3)$
Greeneich and Van Duzer et al.	$MIBK : IPA(1:3)$	$6.8X10^{21}$
Hawryluk et al.	$MIBK : IPA(2:3)$	$1.1X10^{22}$
Kyser and Murata	$MIBK : IPA(1:3)$	$1.1X10^{22}$
Possin and Norton	$MIBK : IPA(1:3)$	$1.5X10^{22}$
Shimzu et al.	$95\%Ethanol$	$2.4X10^{22}$

Table A.1: Threshold energy density (E$_T$) for dissolution of PMMA resist.

Reference	Solvent	Temperature(^{0}C)	R$_0$ (nm/min)	B (nm/min)	A
Hatzakis et al.	MIBK^a	20.5	0	$1.25X10^8$	1.4
Greeneich	MIBK	22.8	8.4	$3.14X10^7$	1.5
Greeneich	$MIBK : IPA(1:1)$	22.8	0	$6.65X10^5$	1.19
Greeneich	$MIBK : IPA(1:3)$	22.8	0	$9.33X10^{13}$	3.86

^{a} Saturated with water; MIBK-methyl isobutyl ketone; IPA-isopropyl alcohol.

Table A.2: Solubility rate constants for PMMA resist.

BIBLIOGRAPHY

[1] P.I. Hagouel, "X-ray lithographic fabrication of blazed diffraction gratings", *PhD Dissertation* , University of California, Berkeley, 1976.

[2] K.K.H. Toh, A.R. Neureuther, and E.W. Scheckler, "Algorithms for Simulation of Three-Dimensional Etching", *IEEE Transactions on Computer-Aided Design*, vol. 13, pp. 616-624, 1994.

[3] R. Jewett, P. Hagouel, A. Neureuther, and T. van Duzer, " Line-Profile Resist Development Simulation Techniques. Polymer Engineering and Science", *IEEE Trans. Comput. Aid. Design*, vol. 17, pp. 381-384, 1977.

[4] Zai-Fa Zhou, Qing-An Huang, Wei-Hua Li and Wei Lu, "A novel 2D dynamic cellular automata model for photoresist etching process simulation", *Journal of Micromechanics and Microengineering*, vol. 15, pp. 652-662, 2005.

[5] D.F. Kyser and N.S. Viswanathan, "Monte Carlo simulation of spatially distributed beams in electron-beam lithography", *Journal of Vacuum, Science and Technology*, vol. 12, pp. 1305-1308, Nov./Dec. 1975.

[6] D.F. Kyser and R.Pyle, "Computer Simulation of Electron-Beam Resist Profile", *IBM Journal Resist Development*, vol. 24, pp. 426-437, July 1980.

[7] Fletcher Jones and Jurij Paraszczak, "RD3D (Computer Simulation of Resist Development in Three Dimensions", *IEEE Transactions Electron Devices*, vol. 28, pp. 1544-1552, Dec. 1981.

[8] F.H. Dill, A.R. Neureuther, J.A. Tuttle, and E.J. Walker, "Modeling Projection Printing of Positive Photoresists", *IEEE Transactions Electron Devices*, vol. 22(7), pp. 456-464, 1975.

[9] Yoshihiko Hirai, Sadafumi Tomida, Kazushi Ikeda, Masaru Sasago, Masayki Endo, Sigeru Hayama, and Noboru Nomura, "Three-Dimensional Resist Process Simulator PEACE (Photo and Electron Beam Lithography Analyzing Computer Engineering System)", *IEEE Transactions on Computer-Aided Design*, vol. 10, pp. 802-807, June 1991.

[10] Ioannis Karafyllidis and Adonios Thanailakis, "Simulation of two-dimensional photoresist etching process in integrated circuit fabrication using cellular automata", *Modeling Simulation Materials Science Engineering*, vol. 3, pp. 629-642, 1995.

[11] J.C.H. Phang and H. AHmed, “Line profiles in thick electron resist layers and proximity effect correction”, *Journal of Vacuum, Science and Technology*, vol. 16, pp. 1754-1758, Nov./Dec. 1979.

[12] Sherry J. Gillespie, “Resist profile control in e-beam Lithography”, *IBM J. Res. Develop.*, pp. 454-460, July 1984.

[13] Y.C. Patil, A. Teolis, D. Park, R. Bass, K. Rhee, B. Bradie, M.C. Peckerar, “An error measure for dose correction in e-beam nanolithography”, *J. Vac. Sci. Technolo.*, B 8(6), Nov./Dec. 1990.

[14] V.V. Aristov, B.N. Gaifullin, A.A. Svinstov, S.I. Zaitsev, H.F. Raith, R. Jede, “Accuracy of proximity effect correction in electron lithography after development”, *J. Vac. Sci. Technolo.*, B 10(6), Nov./Dec. 1992.

[15] Jianyun Zhou, XiaoMin Yang, “Monte Carlo simulation of process parameters in electron beam lithography for thick resist patterning”, *J. Vac. Sci. Technolo.*, B 24(3), May/June 2006.

[16] U. Hofmann, C. Kalus, A. Rosenbusch, R. Jonckheere and A. Hourd, “Hierarchical E-beam Proximity Correction in Mask Making”, *Proceedings of SPIE Conference on E-Beam, X-Ray, EUV, and Ion-Beam Sub-mcrometer Lithographies for Manufacturing VI*, vol. 2723, pp.150-158, March 1996.

[17] M. Peckerar, R. Bass and K, Rhee, “Sub-0.1 u electron-beam lithography for nanostructure development”, *J. Vac. Sci. Technol.* B 18(6), pp.3143-3149, Nov/Dec 2000.

[18] F. Hu and S.-Y. Lee, “Dose Control for Fabrication of Grayscale Structures using a Single Step E-beam Lithographic Process”, *J. Vac. Sci. Technol.*, B 21(6), pp.2672-2679, Nov/Dec 2003.

[19] F. Hu, “An Implementation of Proximity Effect Correction for Grayscale E-Beam Lithography”, *Masters Thesis*, Auburn University, 2002.

[20] V. V. Aristov, S. V. Dubonos, R. Ya. Dyachenko, B. N. Gaifullin, V. N. Matveev, H. Raith, A. A. Svintsov, and S. I. Zaitsev, “Three-dimensional design in electron-beam lithography”, *J. Vac. Sci. Technol.*, B 13(6), pp.2526-2528, Nov/Dec 1995.

[21] S.-Y. Lee and B. Liu, “Region-Wise Proximity Effect Correction for Heterogeneous Substrates in E-Beam Lithography: Shape Modification”, *J. Vac. Sci. Technol.*, B 16(6), pp.3874-3879, Nov/Dec, 1996.

[22] M. Osawa, K. Ogino, H. Hoshino, Y. Machida, H. Arimoto, “3D Proximity Effect Correction Based on the Simplified Electron Energy Flux Model in Electron-Beam Lithography”, *J. Vac. Sci. Technol.*, B 22(6), pp.2923-2928, Nov/Dec, 2004.

[23] M. Osawa, K. Ogino, H. Hoshino, Y. Machida, H. Arimoto, "3D Proximity Effect Correction for Multilayer Structures in Electron-Beam Lithography", *Japanese J. of App. Sci.*, pp.3762-3766, June, 2004.

[24] L. Leunissen, R. Jonckheere, U. Hofmann, N. Unal and C. Kalus, "Experimental and Simulation Comparison of Electron-Beam Proximity Correction", *J. Vac. Sci. Technol.*, B 22(6), pp.2943-2947, Nov/Dec, 2004.

[25] W. Moreau, "Semiconductor Lithography: Principles, Practices, and Materials", Plenum Press, 1988.

[26] S.-Y. Lee and B.D. Cook, "PYRAMID-A Hierarchical Rule-based Approach to Proximity Effect Correction in E-Beam Lithography: Part I - Exposure Estimation", *IEEE Transactions on Semiconductor Manufacturing*, vol. 11, no. 1, pp.108-116, February 1998.

[27] http://www.ics.uci.edu/ eppstein/161/960312.html

[28] T. Chang, "Proximity effect in e-beam lithography", *Journal of Vacuum Science and Technology*, vol. 12, pp. 1271-1275 Nov./Dec. 1975.

[29] M. Parikh, "Correction to proximity effects in electron-beam lithography. II. Implementation", *Journal of Applied Physics*, vol. 50, no. 6, pp. 4371-4382, June 1979.

[30] N. D. Wittels and C. Youngman, "Proximity effect correction in electron-beam lithography", *Proceedings of the 8th International Conference on Electron and Ion Beam Science and Technology*, ed. by R. Bakish, Electrochemical Society, Princeton, New York, pp. 361-365, 1978.

[31] D.P. Kern,"A Novel Approach to Proximity Effect Correction", *Proceedings of the 9th International Conference on Electron and Ion Beam Science and Technology*, ed. by R. Bakish, Electrochemical Society, Princeton, NJ, pp. 326-339, 1980

[32] D. Chow, J. McDonald, C. King, W. Smith and A. J. Steckl, "An image processing approach to fast, efficient proximity effect correction for electron-beam lithography", *Journal of Vacuum, Science and Technology*, vol. 1, pp. 1383-1390, Oct./Dec. 1983.

[33] J. Greeneich, "Proximity effect correction using a dose compensation curve", *Journal of Vacuum Science and Technology*, vol. 19, pp. 1269-1274, Nov./Dec. 1983.

[34] M. Parikh, "Calculation of changes in pattern dimensions to compensate for proximity effects in electron-beam lithography", *Journal of Applied Physics*, vol. 51, pp. 705-709, January 1980.

[35] M. Parikh, "Correction to proximity effects in electron-beam lithography. III. Experiments", *Journal of Applied Physics*, vol. 50, no. 6, pp. 4383-4387, June 1979.

[36] M. Parikh, "Proximity Effect Corrections in Electron Beam Lithography", *Proceeding of the 8th International Conference on Electron and Ion Beam Science and Technology*, ed. by R. Bakish, Electrochemical Society, Princeton, NJ, pp. 382-391, 1978.

[37] S.K.S. Ma, M. Parikh, and W. Ward, "Proximity Corrections in a Raster Scan Electron Lithography Machine", *Journal of Vacuum Science and Technology*, vol. 19, no. 4, pp. 1275-1278, November/December 1981.

[38] W.T Lynch, T.E. Smith, W. Fichtner, "An algorithm for proximity effect correction with E beam exposure", *International Conference on Microlithography*, Microcircuit Engineering, pp. 309-314, October 5-8, 1982.

[39] G. Owen, "Methods for proximity effect correction in electron-beam lithography", *Journal of Vacuum, Science and Technology*, vol. 8, pp. 1889-1892, Nov./Dec. 1990.

[40] S.-Y. Lee, J.C. Jacob, C.M. Chen, J.A. McMillan, and N.C. MacDonald, "Proximity effect correction in electron-beam lithography: A hierarchical, rule-based scheme - PYRAMID", *Journal of Vacuum Science and Technology*, vol. B9, pp. 3048-3053, Nov./Dec. 1991.

[41] J.C. Jacob, S.-Y. Lee, J.A. McMillan, and N.C. MacDonald, "Fast proximity effect correction: An extension of PYRAMID for circuit patterns of arbitrary size", *Journal of Vacuum Science and Technology*, vol. B10, pp. 3077-3082, Nov./Dec. 1992.

[42] J.C. Jacob, "PYRAMID - A hierarchical, rule-based scheme for proximity effect correction in electron-beam lithography: An Implementation for single layer circuits", *Masters Thesis*, Cornell University, 1992.

[43] S.-Y. Lee and B. D. Cook, "PYRAMID - A Hierarchical, Rule-Based Approach Toward Proximity Effect Correction - Part I: Exposure Estimation", *IEEE Transactions on Semiconductor Manufacturing*, Vol. 11, No. 1, pp. 108-116, Feb. 1998.

[44] B. D. Cook and S.-Y. Lee, "PYRAMID - A Hierarchical, Rule-Based Approach Toward Proximity Effect Correction - Part II: Correction", *IEEE Transactions on Semiconductor Manufacturing*, Vol. 11, No. 1, pp. 117-127, Feb. 1998.

[45] B. D. Cook, "PYRAMID - A Hierarchical, Rule-Based Proximity Effect Correction Scheme for electron-beam lithography: Generalization and optimization for homogeneous substrates", *Ph.D. Dissertation*, Cornell University, August 1996.

[46] B. D. Cook and S.-Y. Lee, "Dose, shape and hybrid modifications for PYRAMID in electron beam proximity effect correction", *Journal of Vacuum Science and Technology*, B 15(6), pp. 2303-2308, Nov./Dec. 1997.

[47] B. D. Cook and S.-Y. Lee, "Fast Exposure Simulation for Large Circuit Patterns in Electron Beam Lithography", *Proceddings of the International Conference on Image Processing*, pp. 442-445, October 1995.

[48] B. D. Cook and S.-Y. Lee, “Performance Analysis and Optimal Parameter Selection for PYRAMID”, *Proceddings of the International Conference on Micro- and Nano-Engineering*, pp. 61-64, September, 1995.

[49] S.-Y. Lee and B. D. Cook, “Interior Area Removal Method for PYRAMID”, *Journal of Vacuum Science and Technology*, vol. B12, no. 6, pp. 3449-3454, Nov./Dec. 1994.

[50] B. D. Cook and S.-Y. Lee, “A Quantitative Performance Analysis of PYRAMID”, *Proceddings of the International Conference on VLSI and CAD*, pp. 16-18, November, 1993.

[51] B. D. Cook and S.-Y. Lee, “Fast Proximity Effect Correction: An Extension of PYRAMID for Thicker Resists”, *Journal of Vacuum Science and Technology*, vol. B7, No. 6, pp. 1556-1560, Nov./Dec. 1989.

[52] S.-Y. Lee, B. Liu, B. D. Cook, “Reducing recursive effect for fast proximity correction”, *Microelectronic Engineering*, vol 35, pp. 491-494, 1997.

[53] J. Laddha, “An efficient hierarchical pattern representation format for proximity effect correction in E-beam lithography”, *Masters Thesis*, Auburn University, December 1999.

[54] S.-Y. Lee and J. Laddha, “Adaptive selection of control points for improving accuracy and speed of proximity effect correction”, *Journal of Vacuum Science and Technology*, B 16(6), pp. 3269-3274, Nov./Dec. 1998.

[55] J. Laddha and S.-Y. Lee, “Application of neural network to enhancing accuracy of E-beam proximity effect correction”, *Microelectronic Engineering*, No.53, pp. 317-320, 2000.

[56] S.-Y. Lee, J. Laddha, “Automatic Determination of Spatial Dose Distribution for Improved Accuracy in E-beam Proximity Effect Correction”, *International Conference on Micro and Nano Engineering*, September 2000.

[57] D. He, “An extension of the dose modification pyramid : circuit primitive partitioning and simultaneous correction”, *Master Thesis*, Auburn University, December 2000.

[58] S. Johnson, “Simulation of electron scattering in complex nanostructures: Lithography, metrology and characterization”, *Ph.D. dissertation*, Cornell University, Ithaca, N.Y., Jan. 1992.

[59] P. Rai-Choudhury, “Handbook of Microlithography, Micromachining, and Microfabrication: Volume I”, SPIE Optical Engineering Press: London, UK, Jan. 1997.